MESMERISED: Super-accelerated 7 T STEAM imaging for quantitative multi-contrast and diffusion MRI

F.J. Fritz [a], B.A. Poser [a], A. Roebroeck [a]

[a] *Department of Cognitive Neuroscience, Faculty of Psychology and Neuroscience, Maastricht University, Maastricht, The Netherlands*

Abstract

There is an increasing interest in quantitative imaging of T_1, T_2 and diffusion contrast in the brain due to greater robustness against bias fields and artifacts, as well as better biophysical interpretability in terms of microstructure. However, acquisition time constraints are a challenge, particularly when multiple quantitative contrasts are desired and when extensive sampling of diffusion directions, high b-values or long diffusion times are needed for multi-compartment microstructure modeling. Although ultra-high fields of 7 T and above have desirable properties for many MR modalities, the shortening T_2 and the high specific absorption rate (SAR) of inversion and refocusing pulses bring great challenges to quantitative T_1, T_2 and diffusion imaging. Here, we present the MESMERISED sequence (Multiplexed Echo Shifted Multiband Excited and Recalled Imaging of STEAM Encoded Diffusion). MESMERISED removes the dead time in Stimulated Echo Acquisition Mode (STEAM) imaging by an echo-shifting mechanism. The echo-shift (ES) factor is independent of multiband (MB) acceleration and allows for very high multiplicative (ESxMB) acceleration factors, particularly under moderate and long mixing times. This results in high duty cycle and time efficiency at 7 T, particularly for quantitative T_1 and diffusion imaging, while also retaining the capacity to perform quantitative T_2 and B_1 mapping. We demonstrate the super-acceleration of MESMERISED for whole-brain T_1 relaxometry with total acceleration factors up to 36 at 1.8 mm isotropic resolution, and up to 54 at 1.25 mm resolution qT_1 imaging, corresponding to a 6x and 9x speed-up, respectively, compared to MB-only accelerated acquisitions. We demonstrate quantitative T_2 and B_1 mapping to illustrate multi-contrast mapping with the same MESMERISED sequence and the same readout train. Finally, we demonstrate highly efficient diffusion MRI with high b-values and long diffusion times in two separate cases. First, we show that super-accelerated multi-shell diffusion acquisitions with 370 whole-brain diffusion volumes over 8 b-value shells up to b = 7000 s/mm^2 can be generated at 2 mm isotropic in under 8 minutes, a data rate of almost a volume per second, or at 1.8 mm isotropic in under 11 minutes. Second, we demonstrate time-efficient sampling of different diffusion times with 1.8 mm isotropic diffusion data acquired at four diffusion times up to 290 ms, which supports both Diffusion Tensor Imaging (DTI) and Diffusion Kurtosis Imaging (DKI) at each diffusion time. MESMERISED extends possibilities to efficiently probe T_1, T_2 and diffusion contrast for multi-component modeling of tissue microstructure.

Keywords

Quantitative MRI, Diffusion MRI, Multi-contrast MRI, 7T, Accelerated Imaging, Microstructure

Introduction

Magnetic resonance imaging (MRI) derives most of its versatility as an imaging technique from being able to weight images towards a multitude of contrasts, prominently among which are T_1, T_2/T_2* and diffusion contrasts. Recently, there is an increasing interest in quantitative imaging of these contrasts for two main reasons. First, quantitative T_1, T_2 and diffusion images possess greater robustness against bias fields and artifacts, since the effects of spatially slowly varying radio-frequency (RF) transmit and receive fields are mostly removed. Second, quantitative images have better biophysical interpretability, since they have interpretable physical units. This makes them a better proxy for biological microstructure and phenomena, such as myelin (e.g. Callaghan et al., 2015; Lutti et al., 2014; Weiskopf et al., 2013), g-ratio (e.g. Berman et al., 2019; Campbell et al., 2018), iron (e.g. Fukunaga et al., 2010; Stuber et al., 2014; Weiskopf et al., 2013), axonal density (e.g. Assaf and Basser, 2005; Zhang et al., 2012) or coarse-graining due to random axonal packing (e.g. Novikov et al., 2014). However, since quantitative MRI (qMRI) requires the acquisition of many volumes, from which the quantitative image is then derived, long acquisition times are a challenge, particularly when multiple quantitative contrasts are desired.

Acquisition time constraints are particularly pressing for diffusion MRI (dMRI). The signal varies with the orientation, strength and diffusion time encoded by diffusion gradients, making diffusion contrast inherently multi-dimensional. Moreover, recent developments in biophysical microstructure quantification with dMRI require sampling more of the multi-dimensional contrast space than with older methods. The conventional method for the analysis of white matter in dMRI imaging is the tensor model in Diffusion Tensor Imaging (DTI; Basser et al., 1994; Pierpaoli et al., 1996). Although a DTI derived index variable such as Fractional Anisotropy (FA) is sensitive, it is also unspecific, since differences in FA can reflect different axonal properties such as axon density, diameter distribution and myelination (Assaf et al., 2004; Assaf and Pasternak, 2008; Beaulieu, 2002; De Santis et al., 2014; Jones et al., 2013). Therefore, advances in diffusion microstructure modeling have aimed at greater specificity than DTI in relating the dMRI signal to the underlying cellular microstructure (Alexander et al., 2010; Assaf et al., 2013; Assaf and Basser, 2005; Assaf et al., 2008; Assaf et al., 2004; De Santis et al., 2014; Fieremans et al., 2013; Jelescu et al., 2015; Panagiotaki et al., 2012; Santis et al., 2014; Zhang et al., 2012). Models such as the Neurite Orientation Dispersion and Density Imaging model (NODDI; Zhang et al., 2012), the Combined Hindered And Restricted Model of Diffusion (CHARMED; Assaf and Basser, 2005), and the White Matter Tract Integrity model (WMTI; Fieremans et al., 2013) can provide measures specific to fiber density and orientation dispersion. These require the acquisition of a large number of diffusion directions over multiple b-values, sometimes extending to b-values as high as 6000 - 8000 s/mm^2, leading to acquisition times of 10 - 20 minutes or longer. In addition, sensitivity can be gained to axonal diameter distributions (Alexander et al., 2010; Assaf et al., 2008; De Santis et al., 2016a; Zhang et al., 2011), water-exchange over cell membranes (Li et al., 2016; Nilsson et al., 2013) and coarse-graining effects (Burcaw et al., 2015; Novikov et al., 2014), but this requires the acquisition of a large number of b-values and diffusion times extending to 200 - 800 ms, often leading to acquisition times of 30 - 60 min.

Developments in echo-planar imaging (EPI) acquisition have allowed significant speed-up in the acquisition of volume time series weighted for T_1, T_2/T_2* or diffusion. Prominently among these is multiband (MB) or simultaneous multi-slice (SMS) acquisition (Feinberg et al., 2010; Moeller et al., 2010; Setsompop et al., 2012), which allows 2- to 4-fold speed-up for high flip angle applications at the expense of a higher specific absorption rate (SAR). However, even with MB acceleration,

quantitative multi-contrast studies that require extensive diffusion MRI, as well as mapping of T_1 and/or T_2, are facing prohibitively long acquisition times.

In the domain of high spatial resolution imaging, ultra-high fields (UHF) of 7 Tesla (7 T) and above have enabled efficient high spatial resolution mapping of quantitative T_1 (e.g. Marques et al., 2010; O'Brien et al., 2014), T_2* (e.g. Fukunaga et al., 2010) and diffusion (e.g. Vu et al., 2015). In this work, our main aim was to establish whether the high signal-to-noise ratio (SNR) available at 7 T could be leveraged for highly time-efficient quantitative multi-contrast acquisition at moderate resolutions, particularly when including dMRI at high b-values or long diffusion times. Although UHF has desirable properties for many MR modalities, the shortening of T_2 and the high SAR load of inversion and refocusing pulses bring challenges to efficient quantitative T_1, T_2 and diffusion imaging. Diffusion MRI sequences such as pulsed-gradient spin-echo (PGSE; e.g. Vu et al., 2015) and steady-state free precession (SSFP; e.g. Lu et al., 2012) have been optimized at 7 T to mitigate some of these limitations. However, they remain limited to MB acceleration factors of 2 to 4 (Eichner et al., 2014; Vu et al., 2015; Wu et al., 2013), with SAR as the main limiting factor.

Therefore, we investigated the possibilities of the Stimulated Echo Acquisition Mode (STEAM) sequence (Frahm et al., 1985). The STEAM sequence has some attractive advantages for multi-contrast MRI at UHF. First, it is highly multi-contrast capable, being able to provide quantitative T_1 (qT_1) contrast (by relaxometry on the mixing time, TM), quantitative T_2 (qT_2) contrast (by relaxometry on the echo time, TE), transmit (B_1+) field mapping, and quantitative diffusion contrast. Furthermore, both b-value and diffusion time parameters in dMRI with STEAM can be probed at the high values desirable for many diffusion microstructure applications. Second, both a spin echo (SE) and stimulated echo (STE) signal can be independently acquired after a single excitation pulse, enhancing the capacity for efficient multi-contrast acquisition. Third, STEAM is highly efficient in SAR given its preferred 90°-90°-90° flip angle scheme. It has ~60% of the SAR of a comparable 90°-180° spin-echo sequence and ~33% of the SAR of a comparable 180°-90°-180° inversion-prepared spin-echo sequence (assuming similar slice-selection and a quadratic SAR/flip angle relationship). This also means that applying multiband pulses for SMS imaging is easier to apply for high MB factors in STEAM since SAR increases linearly with MB factor. However, the STEAM sequence also has inherent disadvantages. Both the SE and STE signals have only 50% of the signal level and signal to noise ratio (SNR), compared to the SE from a 90°-180° spin-echo sequence. Moreover, there is a considerable dead time in STEAM (Figure 1A), especially when moderate to long mixing times (useful for T_1-weighting and probing of long diffusion times) are required, which leads to a low SNR per unit time efficiency.

Here, we present the MESMERISED sequence (Multiplexed Echo Shifted Multiband Excited and Recalled Imaging of STEAM Encoded Diffusion). MESMERISED removes the dead time in stimulated acquisition mode (STEAM) imaging by an echo-shifting mechanism. The echo-shift (ES) factor is independent of MB acceleration and allows for very high multiplicative ESxMB acceleration factors, particularly under moderate and long TM's. This results in high duty cycle and high time efficiency at 7 T, particularly for quantitative T_1 and diffusion imaging. We demonstrate the super-acceleration of MESMERISED for whole-brain T_1 relaxometry with total acceleration factors up to 36 for 1.8 mm resolution and up to 54 for 1.25 mm resolution qT_1 imaging. We then demonstrate quantitative T_2 and B_1+ mapping to illustrate multi-contrast mapping with the same MESMERISED sequence. Finally, we demonstrate highly efficient diffusion MRI with high b-values and long diffusion times in two cases: First, we show super-accelerated multi-shell diffusion acquisitions with 370 whole-brain

diffusion volumes over 8 b-value shells up to b = 7000 s/mm^2 at isotropic resolutions of 1.8 mm and 2.0 mm. Second, we demonstrate time-efficient sampling of different diffusion times with 1.8 mm isotropic diffusion data acquired at four diffusion times up to 290 ms.

Theory

The MESMERISED sequence is based on the standard (diffusion-weighted) STEAM sequence (Figure 1A). The STEAM pulse sequence uses three radiofrequency (RF) pulses: excitation (Exc), storing (Sto) and recalling (Rec) pulses, which can create several spin echoes (SE's) and a stimulated echo (STE), and was first introduced by Frahm and colleagues (Frahm et al., 1985). In general terms, the excitation pulse places the magnetization into the transverse plane where it undergoes T_2 decay. Subsequently, the storing pulse places ('stores') part of the total magnetization along the longitudinal axis where it is subject to T_1 decay during the mixing time (TM). The remaining part of the magnetization forms the primary SE signal. Finally, the recalling pulse places ('recalls') the stored magnetization to the transverse plane where it once again undergoes T_2 decay until the STE is formed. This sequence of pulses can create three more SE signals (the second, third and fourth spin-echo) after the STE, which are the consequence of the free induction decay (FID) signal generated by the storing and recalling pulses. We focus on the first or primary SE signal in the remainder of this work and refer to it simply as 'the SE' hereafter. Whereas the SE undergoes only T_2 decay, the STE signal undergoes both T_1 and T_2 decay, because the signal is obtained from spins *stored* along the longitudinal axis for the duration of the TM, during which there is T_1 relaxation. Furthermore, both echoes (SE and STE) share the transverse magnetization created by the excitation pulse and therefore split the total excited signal, which becomes evenly distributed between SE and STE when the storing pulse has a flip angle of 90°.

MESMERISED removes the dead time in STEAM by shifting Exc-Sto pulse pairs and SE readout for one or more MB slice groups into the dead time of earlier slice groups (Figure 1B). We refer to this as echo-shifting, by analogy to sequences that shift sequence elements to achieve echo times longer than their repetition time (TR) in gradient-echo or steady-state free precession sequences (c.f. Ehses et al., 2015; Gibson et al., 2006). However, we note the shifting mechanism here is fundamentally different and does not achieve TE > TR. The echo-shifting in MESMERISED temporally interleaves and multiplexes the contrast evolution of several slices or MB slice-groups. The stored longitudinal magnetization of earlier Exc-Sto and SE readout sequence blocks (SB^A blocks) evolves while later SB^A blocks are executed and SE's are acquired. Subsequently, STE's are recalled and read-out in a sequence of SB^B blocks (Figure 1B), placed at time TM to their corresponding SB^A blocks. We refer to the number of echo-shifted slice groups as the echo-shift factor (ES factor). The echo-shifting is independent of MB acceleration and allows for very high multiplicative ESxMB acceleration factors, particularly under moderate and long TM's. This results in full duty cycle and high time efficiency, particularly for quantitative T_1 and diffusion imaging.

For instance, T_1 relaxometry with STEAM requires a range of TM's acquired under the same TR and TE. Whereas total acquisition time of T_1 relaxometry with MB-STEAM would be determined by the TR of the *longest* TM, acquisition time of T_1 relaxometry with MESMERISED is limited by the TR of *shortest* possible TM. All TM's required for accurately fitting an exponential decay model can be acquired at the full duty cycle and a short TR. Essentially, in MESMERISED a different choice of ES factor determines a simple reordering of the same sequence blocks and enable a different mixing time to be acquired at the same minimized TR (see Supplementary Figure 1).

For diffusion imaging, monopolar diffusion gradient pairs are inserted symmetrically around the storing and recalling pulses. Although only the first (before the storing pulse) and fourth (after the recalling pulse) gradients are needed for diffusion weighting of the STE signal, there are several advantages to a double symmetric placement of four gradients. First, these also serve as crusher gradients at low amplitude and duration in non-diffusion-weighted imaging, helping to remove unwanted echo pathways. Second, the first pair of gradients create a pulsed-gradient spin echo (PGSE) acquisition in the SB^A block, with the corresponding PGSE diffusion contrast in the SE. Third, the second and third gradient act as spoilers during the mixing time for unwanted (secondary and tertiary) spin echo pathways. Additionally, this spoiler action is enhanced in MESMERISED, since the gradients of echo-shifted blocks add to the total spoiler-moment during TM. MESMERISED can acquire diffusion-weighted signals at long diffusion times and high b-values in its STE signal, at relatively low duty cycle demands on the gradients. Besides, it allows highly accelerated probing of multiple diffusion times at the same TR and TE as for T_1 relaxometry, explained above. Finally, as a STEAM variant with both a SE and STE readout, MESMERISED can acquire both a low b-value and short diffusion time (in its diffusion-weighted SE's) and a high b-value and long diffusion time (in its diffusion-weighted STE's) in a single TR.

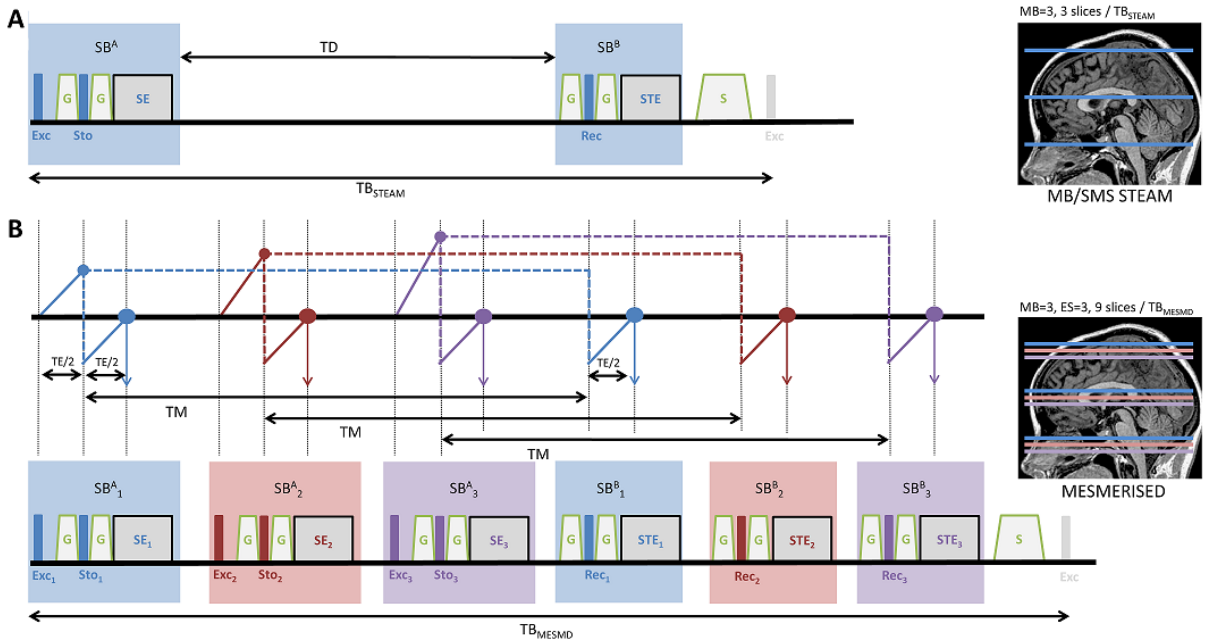

Figure 1: Multiband STEAM (MB-STEAM) versus MESMERISED. (A) A single block (TB_{STEAM}) of the MB-STEAM sequence, consisting of a spin-echo (SE) and stimulated-echo (STE) readout, will acquire MB slices per block, leaving considerable dead time (TD), mostly determined by the desired mixing time (TM). (B) The MESMERISED sequence utilizes this dead time by echo-shifting one or more SB_A blocks (here ES factor 3), resulting in full duty cycle and high time efficiency. The stored longitudinal magnetization of earlier SB_A blocks, illustrated by the dashed horizontal lines in the schematized phase graphs, evolves while later SB_A blocks are executed and SE_i's are acquired. Subsequently, STE_i's are read-out in the SB_B blocks. MESMERISED will acquire ESxMB slices per TB_{MSMD}, which is slightly longer than TB_{STEAM}. Exc/Sto/Rec: spatially selective Excitation/Storing/Recalling pulse; TE: echo time; G: diffusion/crusher gradient; S: spoiler gradient; SB: sequence block.

Methods

MESMERISED sequence implementation

The MESMERISED sequence was implemented on a Siemens 7 T MAGNETOM platform (Siemens Healthineers Erlangen, Germany). A sequence unit (or building block) was created consisting of a single multiband selective pulse surrounded by two gradient pulses and followed by an echo-planar imaging (EPI) readout. This unit serves both as an SB^B block and, preceded by a matched multiband pulse, as an SB^A block (Figure 1B). Blipped-CAIPIRINHA simultaneous multi-slice reconstruction (Setsompop et al., 2012) with the split-slice GRAPPA leak-block approach (Cauley et al., 2014) was performed by using the online reconstruction that is part of the MGH SMS-EPI release for Siemens platforms (https://www.nmr.mgh.harvard.edu/software/c2p/sms). In-plane acceleration was reconstructed with GRAPPA (Griswold et al., 2002) using FLEET autocalibration scans as described in (Blazejewska et al., 2017). The MESMERISED implementation allows for user-controllable MB, GRAPPA and ES acceleration factors, along with the common parameters (TE, TR, number of slices, and resolution parameters: slice thickness, in-plane resolution, readout bandwidth). For diffusion imaging, duration δ, amplitude |G| and time spacing Δ of the diffusion gradient pairs are user-controllable to determine b-value and diffusion time for the SE (b_{SE} and Δ_{SE}= Δ) and the STE (b_{STE} and Δ_{STE}= Δ+TM). Diffusion gradient direction tables were implemented as multiples of 12 directions (24, 36, 48, 60) distributed around a full sphere by an electrostatic repulsion algorithm (Jones, 2004), interspersed with b_0 volumes every 12 directions. Multi-shell tables were implemented by combining tables and suitable modulation of |G| by scaling the length of the diffusion direction vector. To remove the need for SAR-intensive fat saturation (FatSat) pulses, “fat-unfocusing” as described in (Ivanov et al., 2010) was achieved by the appropriate setting of the pulse lengths and bandwidth-time product (BWTP).

MRI data acquisition

Whole-brain acquisitions were performed on a whole-body research 7 T Siemens MAGNETOM (Siemens Healthcare, Erlangen, Germany) system with gradients delivering 70 mT/m maximum strength at a maximum slew rate of 200 T/m/s per physical axis. For RF transmission and reception, a single-channel-transmit/32-channel-receive head coil (Nova Medical, Wilmington, MA, USA) was used. Written informed consent was obtained from all the subjects before imaging and all procedures were approved by the Ethics Review Committee Psychology and Neuroscience (ERCPN) of the faculty of Psychology and Neuroscience, Maastricht University. MESMERISED was tested on five healthy subjects (3 males and 2 females, average weight 75 +- 5 kg and age 29 +- 3 years). Dielectric pads (Teeuwisse et al., 2012) were used to improve B_1+ field homogeneity by positioning two pads at the ears/temples. All sessions started with a localizer scan in three orthogonal directions. Subsequently, a B_0 fieldmap was acquired (Cusack and Papadakis, 2002) and used to optimized B_0 shim currents. An absolute B_1+ map (using a pre-saturation turbo-flash (PreSat-TFL) sequence; Chung et al., 2010) was then acquired and used to calibrate the global transmit flip angle.

Subsequently, MESMERISED acquisitions were performed with full brain coverage, with slices in a transverse orientation. EPI readout was executed along the anterior-posterior (AP) direction, and undersampled with GRAPPA acceleration factor 2 or 3 and using a partial Fourier factor of 6/8. In-plane reference (ACS) lines for GRAPPA (24 lines for factor 2, 36 lines for factor 3) were acquired using FLEET at a flip angle 12° with 2 to 5 dummy pre-scans. For blipped CAIPI MB (Breuer et al., 2006; Setsompop et al., 2012), a CAIPI-shift (CS) factor was employed (MB: 3, CS: 2; and MB: 4, CS: 3). Every acquisition was accompanied by 5 volumes with a reversed-phase encoding direction

(posterior-anterior) only for the contrast with highest signal (i.e. shortest TM or TE, flip angles 90°-90°-90°, and/or b_0 acquisition), used for correction of off-resonance distortions.

MESMERISED protocols were created for imaging of quantitative T_1 (qT_1), quantitative T_2 (qT_2), transmit field (B_1+) mapping and diffusion. In MESMERISED the number of slices must be an integer multiple of MBxES for all employed MB and ES factors. For qT_2, B_1+ and diffusion protocols with a single mixing time or diffusion time this provides a single constraint. For qT_1 or diffusion protocols with multiple TM or diffusion times (Δ), this provides a set of constraints, one for each ES/TM combination. These constraints are easily solved by choosing slice numbers N with a large number of integer divisors (highly composite numbers), such as 60, 72, 90 and 108, which can be used for isotropic imaging resolutions of 2 mm, 1.8 mm, 1.5 mm, and 1.25 mm, respectively. Each integer divisor of slice number divided by MB factor (i.e. N/MB), then determines an allowable ES factor under the same TR (because it determines a single temporal reordering of sequence blocks, see Supplementary Figure 1). For instance, at 72 slices with MB = 3, N/MB = 24 the allowable ES factors are [1, 2, 3, 4, 6, 8, 12, 24]. At full duty cycle, each such ES is associated with a single minimum TM, determined by the length of RF pulses, gradient pulses, and EPI train length. Again due to MESMERISED's temporal block reordering property, the minimum TM for each allowable ES is (very close to) $ES*TM_{ES=1}$, i.e. an integer multiple of the minimum TM for ES = 1.

A proof of principle test was performed to demonstrate that MESMERISED's echo-shifting does not affect the resulting SE and STE images, and therefore the same signal can be acquired in shorter total acquisition time. Sets of MESMERISED SE and STE images were acquired at 1.8 mm isotropic resolution at different ES but fixed TM = 300 ms, TR = 11.88 s and TE = 47.5 ms. ESxMB combinations of 1x3, 2x3 and 4x3 were acquired with transverse slices, GRAPPA 2, FoV 230 x 230 mm^2 and partial Fourier 6/8. The achievable (but unused) minimum TR for ESxMB= 2x3 and 4x3 were recorded to quantify the acceleration potential of MESMERISED.

Quantitative T_1 imaging was performed at 1.8 mm isotropic and 1.25 mm isotropic, by performing relaxometry over a range of allowable ES/TM combinations at the same TR and TE. Five repetitions of each TM were acquired to assess retrospectively what level of data averaging (1, 3 or 5 repetitions) supports robust exponential T_1-decay model fitting. Additionally, T_1 relaxometry was performed at both at the minimum possible TR, at full duty cycle and acceleration, and with a doubling of TR and all TM's. This was done to assess the range of TM's necessary for robust exponential T_1-decay model fitting. Full acquisition parameters are given in Supplementary Table 1.

Quantitative T_2 and B_1+ mappings were performed at 1.8 mm by relaxometry on a range of TE's, and by cosine model fitting of Exc-Sto-Rec = α°- 2α°- α° for a range of multipliers α (Lutti et al., 2012), respectively. Additionally, T_2 relaxometry was performed at both ES = 1 and at ES = 3, to assess whether robust qT_2 mapping can be performed under echo-shifting. Full acquisition parameters are given in Supplementary Table 2.

Multi-shell diffusion imaging was performed at 2.0 mm and 1.8 mm isotropic for different maximum b-values. Diffusion acquisitions were designed to explore the strengths of MESMERISED in achieving a high number of volumes per unit time, and either high b-values or a large range of Δ's. A set multi-shell diffusion acquisitions with maximum b-value 7000 s/mm^2, 185 directions over 4 shells (a total of 370 SE and STE volumes), were performed at 1.8 mm isotropic and different ES/TM, realizing different diffusion times between 80 ms and 430 ms in the STE. A 4-shell acquisition at 2 mm isotropic with maximum b-value 7000 s/mm^2 was performed to explore the effect of a very short TR

(2.36 sec) and a very high number of volumes per unit time. An acquisition at 1.8 mm isotropic at four different diffusion times and two different b-values (1000 and 2500 s/mm^2) was performed to assess efficient exploration of diffusion-time dependent effects on mean diffusivity and mean kurtosis. Full acquisition parameters are given in Supplementary Table 3.

Image processing and analysis

Each MESMERISED dataset (all repetitions for all TM's (qT_1), TE's (qT_2), flip angles (B_1+), or directions and b-values for diffusion) was individually denoised, separately for the SE volumes and STE volumes. Denoising was performed before any other step following the approach by Veraart et al. (2016), using the mrdenoise tool in MRtrix 3.0 (Tournier et al., 2019) with a kernel size of 5 or 7. Subsequently, the data were corrected for movement, off-resonance and eddy-current artifacts using the Topup and Eddy tools of FSL v6.0.1 (Jenkinson et al., 2012). Given that the TE, EPI readout-train, and crushing/diffusion gradients are exactly matched between SE and STE within each acquisition, distortion estimation can be performed on either SE or STE. Therefore, topup was performed on the highest signal SE volumes (i.e. shortest TE, flip angles 90°-180°-90°, and/or b_0 acquisition) and eddy was performed separately on SE and STE volumes with this Topup input. Since data was acquired with shortest-TM volumes first, the first acquired SE and STE volumes are already in close spatial alignment (having been acquired ~ 100 - 300 ms apart in time), which ensures good alignment of all SE and STE volumes. After correction, the following analyses were performed.

qT_1 and qT_2 analysis

For qT_1 analysis, two distinct relaxometry approaches were used which fit volumes at varying TM with the same TR and TE. In the first approach, only the STE volumes are used. The STE signal as a function of TR, TM, TE and flip angles can be written:

$$S_{STE}(TR, TM, TE, \alpha_i) = \frac{1}{2} S_0 \left(1 - \exp\left(-\frac{TR-TM}{T_1}\right)\right) \sin(\alpha_1) \sin(\alpha_2) \sin(\alpha_3) \exp\left(-\frac{TM}{T_1}\right) \exp\left(-\frac{TE}{T_2}\right) \quad (1)$$

Where S_0 contains all parameters not varying with TR, TM, TE and flip angles, such as proton density and Tx/Rx spatial sensitivity profiles, and α_1, α_2, and α_3 are the flip angles (in radians) of excitation, storing, and recalling pulse, respectively. Absorbing all terms that do not vary with TR or TM into the S_0 term, we get:

$$S_{STE}(S_0, TM, TR, T_1) = S_0(\alpha_i, TE, T_2) \left(1 - \exp\left(-\frac{TR-TM}{T_1}\right)\right) \exp\left(-\frac{TM}{T_1}\right) \quad (2)$$

In the first approach, equation 2 was fitted to STE volumes at varying TM and maps for S_0 and T_1 were obtained. In this approach, the S_0 absorbs effects of flip angle and T_2 decay (as well as RF receive coil sensitivities and proton density), and the fitted curve is a product of exponentials.

In the second approach, both SE and STE volumes are used. The SE signal and STE/SE signal ratio as a function of TR, TM, TE and flip angles can be written:

$$S_{SE}(TR, TM, TE, \alpha_i) = S_0 \left(1 - \exp\left(-\frac{TR-TM}{T_1}\right)\right) \sin(\alpha_1) \sin\left(\frac{\alpha_2}{2}\right)^2 \exp\left(-\frac{TE}{T_2}\right) \quad (3)$$

$$\frac{S_{STE}}{S_{SE}} = \frac{\sin(\alpha_2)\sin(\alpha_3)}{1-\cos(\alpha_2)} \exp\left(-\frac{TM}{T_1}\right) \quad (4)$$

Absorbing all terms that do not vary with TR or TM for the ratio into an S^*_0 term, we get:

$$\frac{S_{STE}}{S_{SE}} = S_0^*(\alpha_i)\exp\left(-\frac{TM}{T_1}\right) \quad (5)$$

In the second approach equation 5 was fitted to STE/SE ratio volumes at varying TM and maps for S_0^* and T_1 were obtained. In this approach, the S_0^* absorbs effects of flip angle, and the fitted curve is a simple exponential. Therefore, the second approach uses the available SE images in MESMERISED to establish a potentially lower complexity fit (simple exponential vs. product of exponentials in the first approach). Approach 1 and 2 were both evaluated for the estimation of qT_1 maps and compared for the precision of their estimates by evaluating Fisher Information Matrix (FIM) local uncertainty ((Harms et al., 2019)). In addition, the uncertainty of qT_1 estimates was evaluated for an increasing number (1, 3, 5) of repetitions per TM volume. For qT_2 mapping only the SE signal was used for both acquisitions (ES = 1 and 3) separately, fitting a simple exponential decay of TE's to estimate a qT_2 map.

B1+ analysis

For B_1+ mapping, the approach used by (Lutti et al., 2012) was used on the acquired varying flip angle data. It consisted in taking the ratio between STE and SE signals, where the flip angle ratio between the three STEAM pulses is α°- 2α°- α° (e.g. for α = 90°: 90°-180°-90° degrees for excitation, storing and recalling pulses respectively). The STE/SE ratio is proportional to the cosine of the excitation flip angle:

$$\frac{S_{STE}}{S_{SE}}(\alpha) = S_0\frac{\sin(2\alpha)\sin(\alpha)}{\sin(\alpha)^2}\exp\left(-\frac{TM_0}{T_1}\right) \rightarrow S_0^*(TM_0, b_0)\cos(\alpha) \quad (6)$$

Therefore, the relative B_1+ map can be estimated from a sufficient number of ratio volumes with varying α.

Diffusion analysis

For diffusion MRI, the following analyses were performed. For the 4-shell (max b = 7000 s/mm^2) single-TM acquisitions, the diffusion data from the STE signal was analyzed by DTI on the 1st shell, Diffusion Tensor Kurtosis (Jensen et al., 2005) on the 1st and 2nd shell, Ball&Stick models (Behrens et al., 2007; Behrens et al., 2003) with one (B&S_{r1}), two (B&S_{r2}) and three (B&S_{r3}) sticks on all shells, NODDI model (Zhang et al., 2012) on the 1st and 2nd shell, CHARMED model (Assaf and Basser, 2005) with one ($CHARMED_{r1}$) and two ($CHARMED_{r2}$) cylinder compartments on all shells. For the SE volumes from the same acquisitions, the highest b-value shell was analyzed with DTI. For the 2-shell multi-TM acquisition, both DTI (1st shell) and DKI (1st and 2nd shell) analysis were applied to the STE signal.

Model optimization

All modeling analyses above were performed in the Microstructure Diffusion Toolbox (MDT; https://mdt-toolbox.readthedocs.io/en/latest_release/) with Powell optimizer at patience 10, and using a cascaded optimization approach (Harms et al., 2017). For diffusion modeling, the cascade consisted of: S_0 estimation – B&S_{r1} estimation – desired model; for qT_1, qT_2 and B_1+ analysis, the cascade consisted of: S_0 estimation – desired model. Where relevant, the precision of estimates was evaluated by computing standard deviations derived from the FIM (Harms et al., 2019) .

Results

Figure 2 shows a comparison between image and signals obtained using MESMERISED with no ES (ESxMB = 1x3, equivalent to MB STEAM, cf. Figure 1A), ESxMB = 2x3 and 4x3 for the SE and STE images. Qualitatively, Figure 1A shows that images retain the same contrast and characteristics when dead time is filled up through echo-shifting. At the same time, the minimum TR (minTR) illustrates that MESMERISED allows these images to be acquired at higher acceleration in a shorter time, going from a 11.88 s minTR with ESxMB = 1x3, to 4.83 s minTR with ESxMB = 4x3. Here we should note that, if the shorter TR is actually used, the contrast and SNR might change compared to the long TR images shown here due to magnetization and steady-state effects. The minTR also illustrates that although the additional acceleration compared to multiband STEAM is significant (e.g. 2.46x for ESxMB = 4x3 compared to ESxMB = 1x3), and multiplicative with MB factor (e.g. 7.38x for ESxMB = 4x3 compared to ESxMB = 1x1), the temporal acceleration factor is generally not linear with ES, due to the time added by the SB^{B}_{i} (i> 1) blocks (c.f. Figure 1B). Figure 1B shows a more direct comparison in signal line plots. MESMERISED accelerated signals (2x3 and 4x3) follow the MB STEAM signal (1x3) closely.

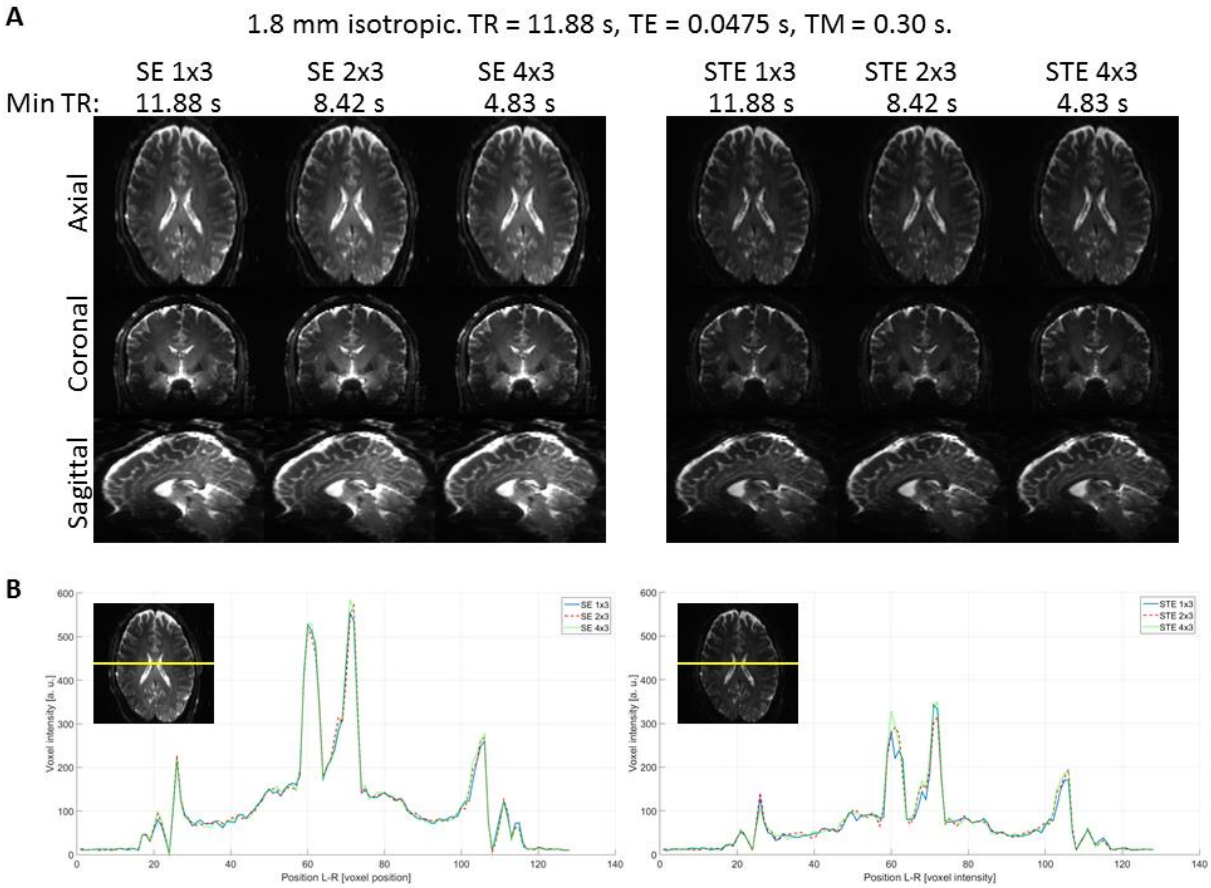

Figure 2: (A) Comparison of MESMERISED images at 1.8 mm isotropic, acquired with MB = 3 at different echo-shifts factors of ES = 1, ES = 2 and ES = 4 but otherwise identical parameters (TR = 11.88 s; TE = 47.5 ms; TM = 300 ms). Left: spin-echo, right: stimulated echo. The minimal achievable TR (min TR) is indicated to illustrate increased acceleration capability with ES > 1. (B) Corresponding signal line plots (see insert) for SE (left) and STE (right) for the three echo-shifts.

qT_1 mapping

Figure 3A shows MESMERISED T_1 relaxometry data at 1.8 mm isotropic. The relaxometry on TM is performed at constant TE (28 ms) and TR (6.9 s) by increasing the ES factor proportionally to TM, for TM's from 140 ms to 1680 ms (see Supplementary Table 1). This results in total acceleration factors (ESxMB) from 3 to 36, highlighting the super-acceleration capability of MESMERISED for T_1 relaxometry. For MB-STEAM and STEAM (without MB) the TR for relaxometry would be limited by the largest TM and would equal 41.51 and 124.60 s, respectively, which means that relative temporal speed-ups of 6.02x and 18.06x are achieved compared to MB-STEAM and STEAM, respectively. Figure 3B shows the whole-brain isotropic resolution S_0 and qT_1 maps resulting from analysis of STE data (i.e. using Equation 2). The S_0 map estimated in this way retains strong T_2 weighting (along with weighting for proton density and Tx/Rx fields), which is apparent in the contrast between white matter (WM) and gray matter (GM) structures. The qT_1 map also shows a high contrast level due to the quantitative differences in T_1 between WM and GM structures. For comparison, Figure 4A shows S_0^* and qT_1 maps resulting from analysis of the STE/SE data from the same acquisition (i.e. using equation 5). The resulting qT_1 map is qualitatively highly similar. However, the theoretical expectation (described above) that the S_0^* map is more weighted for Tx field (i.e. local flip angle) and less for T_2 compared to the S_0 map is borne out in a decreased WM/GM contrast and an increased central darkening strongly (anti-)correlated with the transmit field (described below).

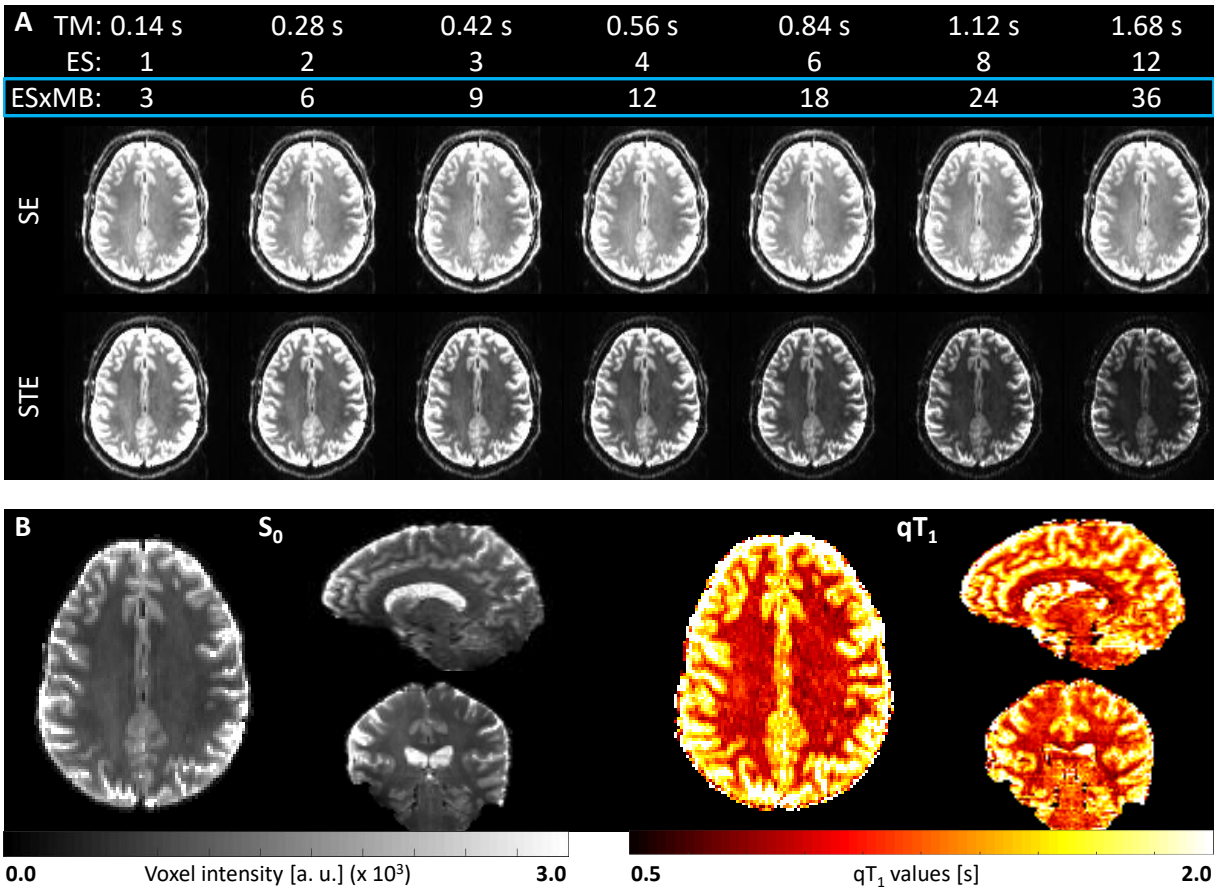

Figure 3: MESMERISED qT_1 mapping and T_1w relaxometry data at 1.8 mm isotropic. (A) Highly accelerated T_1w data was acquired by increasing ES factor in tandem with TM to keep the TR constant and short TM, ES and total acceleration factor EsxMB are given. The acquired SE and STE signals are shown with the STE signal visibly attenuating with TM. (B) The corresponding S_0 (left) and qT_1 (right) maps estimated from the STE signal only (Equation 2).

Figure 4B shows MESMERISED S_0^* and qT_1 maps at 1.25 mm isotropic, from data at constant TE (31.7 ms) and TR (8.8 s), resulting in total acceleration factors (ESxMB) from 3 to 54 over 8 different TM's (Supplementary Table 1). For MB-STEAM and STEAM (without MB) the TR for relaxometry would be limited by the largest TM and would equal 79.79 and 239.40 s, respectively, which means that relative temporal speed-ups of 9.07x and 27.20x are achieved compared to MB-STEAM and STEAM, respectively. A more detailed comparison of the uncertainty of qT_1 maps for the more SNR challenged 1.25 mm isotropic data is shown in Supplementary Figure 2. This shows that uncertainty in qT_1 estimates is lower 1) with an increasing number of repetitions, 2) at long TR (8.8 s) and maximum TM (max TM, 2.16s) compared to short TR (4.4 s) and max TM (1.08 s), and 3) with STE/SE ratio analysis compared to STE-only analysis. Although 1) and 2) are expected given the averaging effect of repetitions and a TM range that is better for the expected T_1's at 7 T (1 - 1.5 s), the benefit of STE/SE ratio analysis is more interesting. With the STE/SE ratio analysis the local maxima in uncertainty for the long TR, TM data is at a similar level with a single repetition (acquisition time 1:40) as for the STE-only analysis with 5 repetitions (acquisition time 6:22); the STE/SE ratio analysis with three repetitions (acquisition time 4:01) has lower uncertainty everywhere (Supplementary Figure 2, bottom row). Additionally, the uncertainty for STE/SE ratio analysis is more homogenous over the brain. Therefore, the 1.25 mm isotropic whole-brain qT_1 map in Figure 4 can be achieved in 2-4 minutes, and the 1.8mm isotropic qT_1 map in 1-2 minutes, depending on the desired precision level.

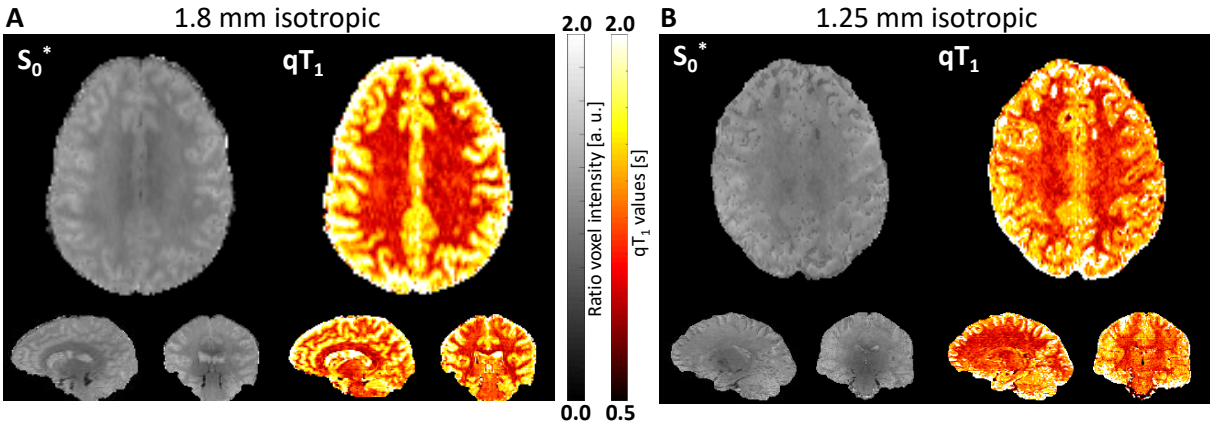

Figure 4: MESMERISED qT_1 mapping at 1.8 mm (A) and 1.25 mm (B) isotropic using the STE/SE ratio T_1-relaxometry model (Equation 5) on data acquired using 3 repetitions (TA: 2:07 and 4:01 min, respectively).

qT_2 and B_1 mapping

Figure 5 shows T_2 relaxometry results and qT_2 maps at 1.8 mm isotropic with MESMERISED both at ES = 3 and ES = 1 (i.e. MB-STEAM). Figure 5A shows SE volumes over echo times of 28.3 ms to 88.3 ms (see Supplementary Table 2) illustrating T_2 decay, qualitatively similar for ES 1 and ES 3. Figure 5B shows the derived qT_2 maps for each ES factor. Analogous to Figure 2, neither the SE signal nor the qT_2 map seem affected by the echo-shifting mechanism in MESMERISED.

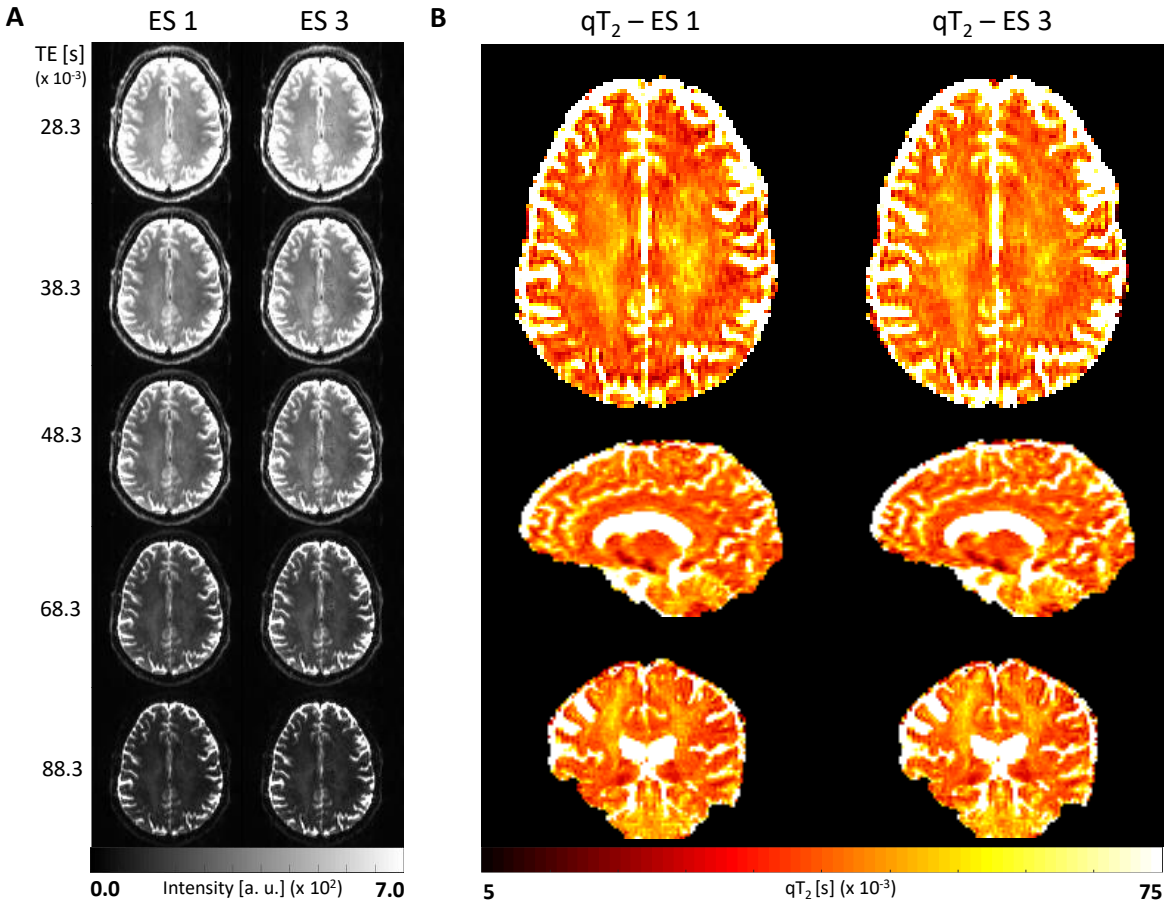

Figure 5: MESMERISED qT_2 mapping and T_2w relaxometry data at 1.8 mm isotropic resolution. (A) Acquired SE volumes for different echo times showing attenuation with TE, for both ES = 1 (left) and ES = 3 (right). (B) The corresponding qT_2 maps for ES = 1 (left) and ES = 3 (right).

Figure 6 shows MESMERISED B_1^+ mapping at 1.8 mm isotropic, derived from both the SE and STE volumes (Figure 6A) for different α_{TX} multipliers in an α_{TX} - $2\alpha_{TX}$ - α_{TX} flip angle scheme for Exc – Sto – Rec pulses. Figure 6B shows the corresponding SE/STE ratios used for B_1^+ map fitting, and Figure 6C depicts the resulting whole-brain relative B_1^+ map. Both the results in Figure 5B and 6C were derived from 3 repetitions per volume, which means that qT_2 and B_1+ mapping can each be achieved in roughly 2 minutes, independently of echo-shift factor used. Here it is important to note that qT_2 and B_1+ mapping, per se, do not benefit from the acceleration by echo-shifting in MESMERISED. However, the ability to perform fast qT_2 and B_1+ mapping with the same pulse sequence that provides accelerated qT_1 and diffusion imaging can have considerable advantages for fast multi-contrast mapping.

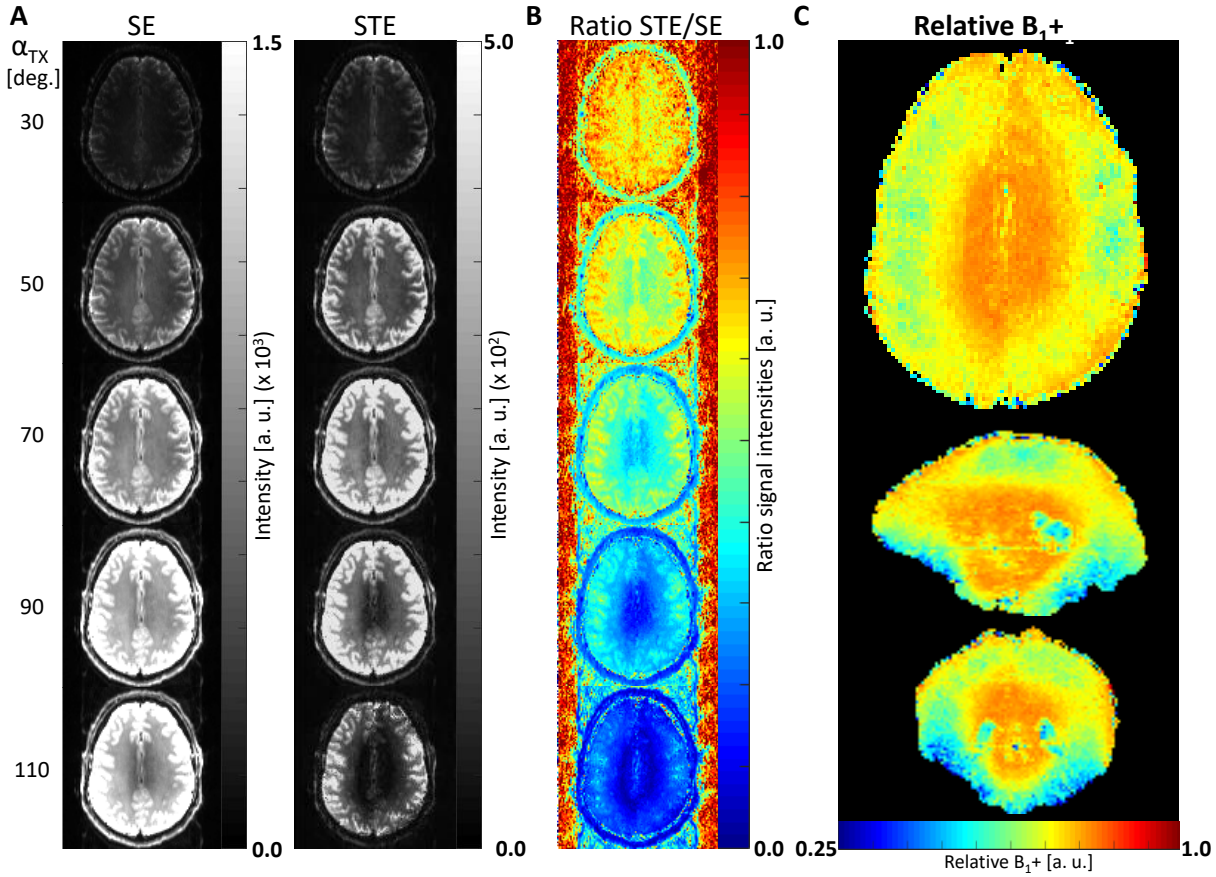

Figure 6: MESMERISED B_1^+ mapping at 1.8 mm isotropic. (A) Acquired SE (left) and STE (right) volumes for different α_{TX} multipliers (B) The corresponding SE/STE ratios used for B_1^+ map fitting (C) The resulting whole-brain relative B_1^+ map.

Diffusion MRI

Figure 7 illustrates the two-dimensional parameter space of diffusion time (vertical) and b-value (horizontal) with MESMERISED diffusion data at 1.8 mm isotropic (where the further 2 dimensions of diffusion direction on the sphere are left implicit). Here, different diffusion times were realized by varying TM and utilizing the maximum echo-shift factor allowed at each TM, individually minimizing TE and TR. All optimized TR's are close to 3.4 s (see Supplementary Table 3), showing a capacity to explore high b-values, up to 7000 s/mm^2, and high diffusion times, up to 436.9 s, at very high acceleration and data rate. In the following, we first focus on the possibilities afforded by multi-shell acquisitions at a single diffusion time and then demonstrate the possibilities of acquisitions at varying diffusion time.

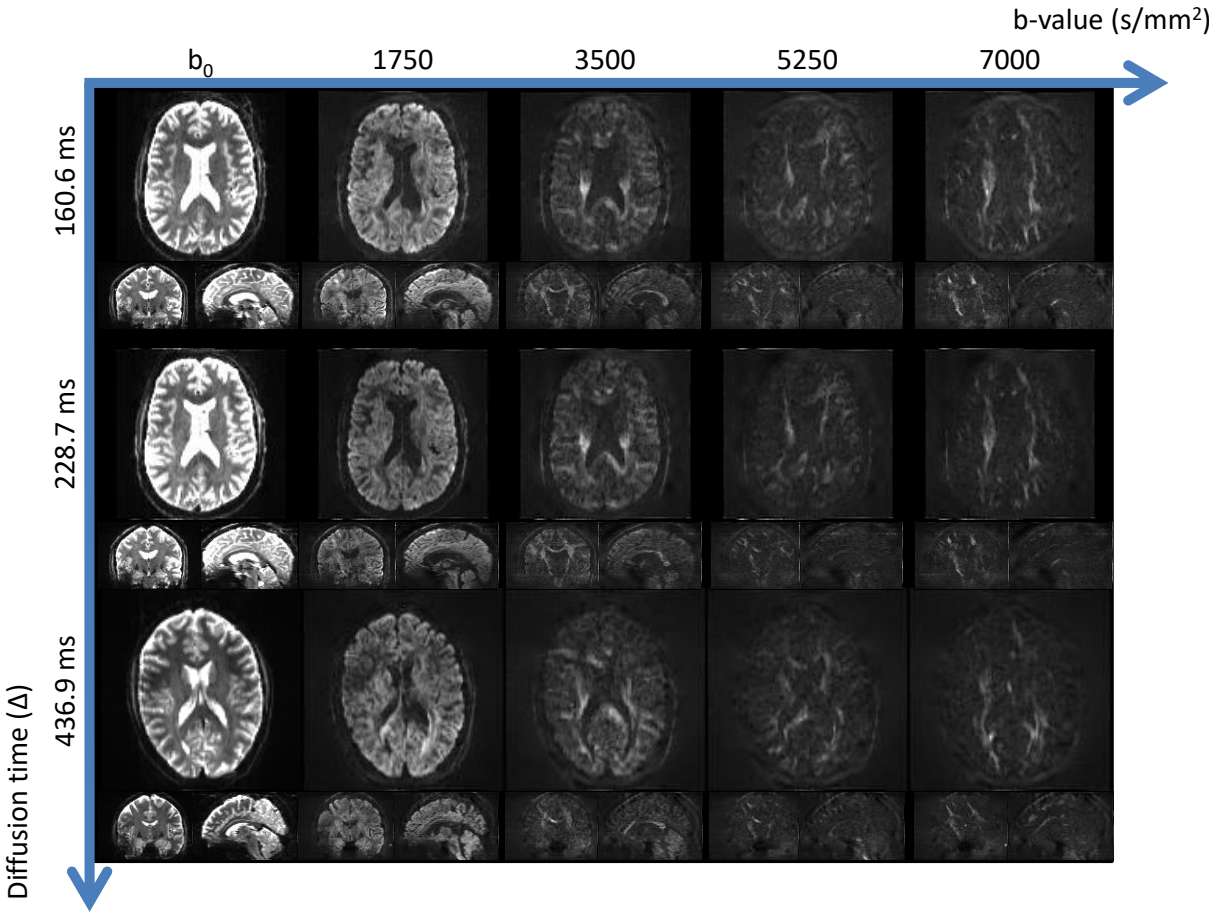

Figure 7: MESMERISED diffusion data at 1.8 mm isotropic spanning the space of diffusion time (vertical) and b-value (horizontal). Whole-brain STE images are shown for three different diffusion times, each corresponding to a distinct ES factor (2 for 160.6 ms, 3 for 228.7 ms, and 6 for 436.9 ms) and individually optimized TE and TR, with different b-values from the same multi-shell acquisition. Simultaneously acquired SE images are not shown.

Multi-shell diffusion MRI

Figure 8 shows example slices out of a 4-shell MESMERISED acquisition and analysis results for the simultaneously acquired STE images (at a diffusion time of 160.6 ms and b-values up to 7000 s/mm^2) and SE images (at a diffusion time of 20.6 ms and b-values up to 752 s/mm^2). This makes explicit how the acquisition of both diffusion-weighted SE volumes and STE volumes provides 8 useful shells of diffusion data in a 4-shell acquisition, even when analyzed separately. Whereas the low-b SE volumes support analysis with Gaussian diffusion models such as the DTI model, the high-b STE volumes are suitable for non-Gaussian diffusion models, such as the DKI, NODDI and CHARMED models. This data was acquired at ES = 2 at a TR of 3.45 s and a TE of 49.8 ms, which tunes the diffusion time of the STE volumes to the shorter end of the achievable range and the b-values of the SE volumes to the higher end, which is accompanied with a higher TE. When a longer diffusion time and higher echo-shift factor is chosen for the same STE volume maximum b-value (e.g. 7000 s/mm^2 here), diffusion gradient length δ naturally decreases, along with the SE maximum b-value (see Supplementary Table 4).

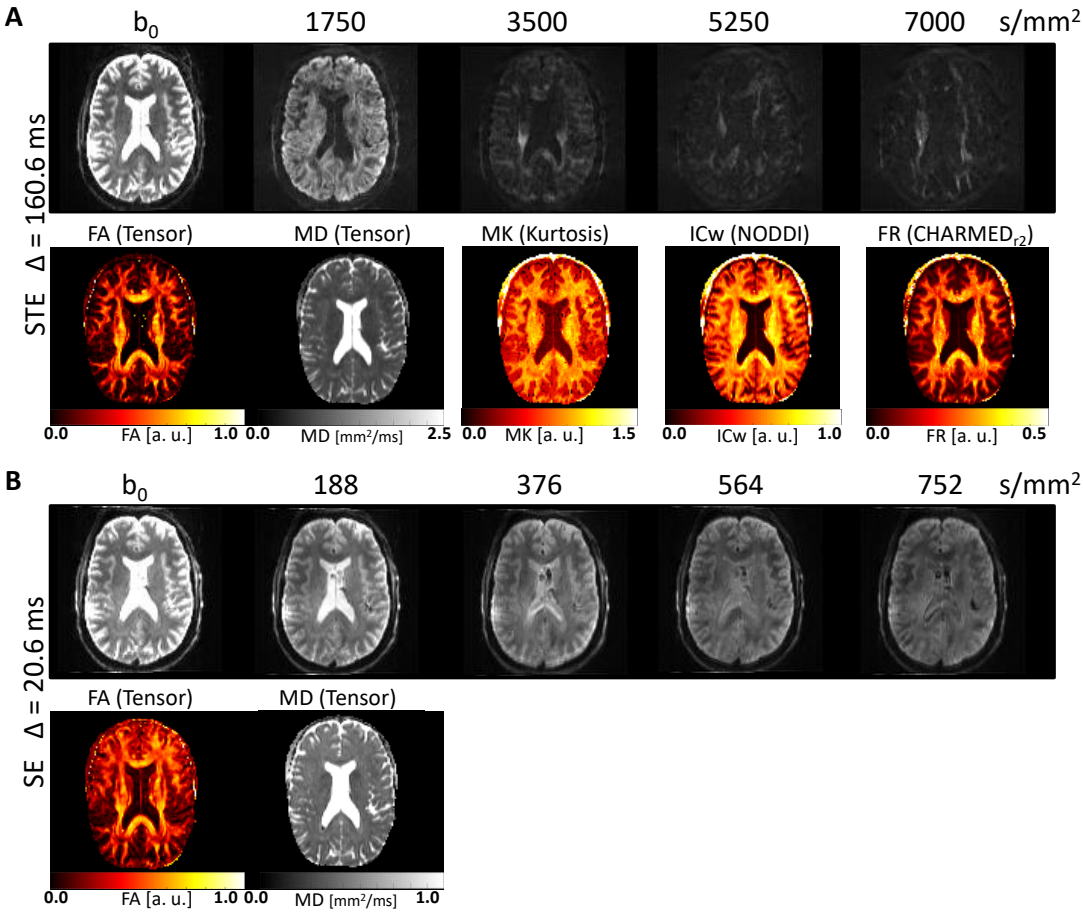

Figure 8: MESMERISED data and diffusion modeling results for simultaneously acquired STE volumes (at high b-values and diffusion time 160.6 ms) and SE volumes (at low b-values and diffusion time 20.6 ms) at 1.8 mm isotropic (ES = 2, TR = 3.45 s, TA = 11:08). (A) Example transverse slices through STE volumes at each b-value in the 4-shell (168 direction) acquisition (top) and their analysis with Tensor, Kurtosis, NODDI and CHARMED models (applied to suitable combinations of shells, bottom). (B) Example transverse slices through SE volumes at each b-value in the 4-shell (168 direction) acquisition (top) and their analysis with the Tensor model (bottom).

Figure 9A shows two 4-shell (max-b = 7000 s/mm^2) acquisitions which realize full duty cycle at similar mixing and diffusion time at 2 mm isotropic (ES = 5, TM = 290 ms; top) and 1.8 mm (ES = 4, TM = 280 ms; bottom). The 2 mm acquisition achieves this at a shorter TR (2.36 s vs. 3.37 s) and therefore enables a higher data rate of ~ 1.2 s per volume (SE and STE together), which generates the full 370 volume dataset in an acquisition time of 7 min and 47 s (vs. 10 min and 53 s for 1.8 mm). Figure 9B shows analysis results for two 4-shell acquisitions with matched full-duty cycle TR (3.45 s) and acquisition time (11:08) at 1.8 mm with different echo shift factors (2 vs. 3) and mixing times (140 ms vs. 210 ms). Besides a different diffusion time for the STE volumes, this also achieves a different maximum b-value for the SE volumes (see Supplementary Table 4). As shown below, the capability to realize different diffusion times for the STE volumes at the same TR opens the possibility to explore diffusion times (when the TE and δ are kept constant at the same b-value) rather than b-values (at the same diffusion time).

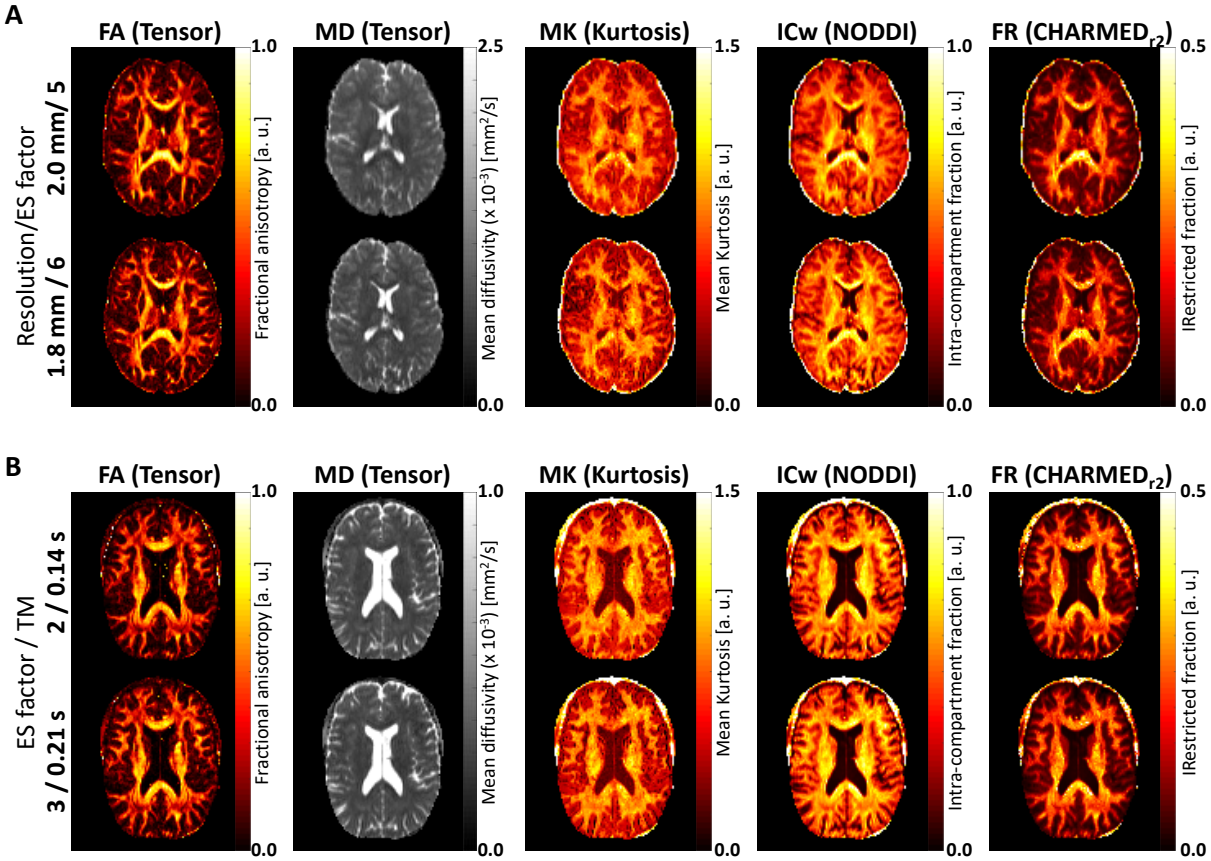

Figure 9: MESMERISED diffusion modeling results for 185 direction multi-shell MESMERISED diffusion acquisitions at different resolutions and diffusion times. (A) Analysis results for Tensor, Kurtosis, NODDI and CHARMED models (applied to suitable combinations of shells) for 2.0mm isotropic (ES = 5, TR = 2.36 s, TA = 7:47) and 1.8 mm isotropic (ES = 6, TR = 3.37 s, TA = 10:53) in the same subject. (B) The same analyses for TM = 140 ms (ES = 2, TR = 3.45 s, TA = 11:08) and TM = 210 ms (ES = 3, TR = 3.45 s, TA = 11:08) at 1.8 mm isotropic in the same subject.

Varying diffusion time

Analogous to keeping TR constant in MESMERISED T_1 relaxometry (by increasing ES factor proportionally to TM), different diffusion times for the STE volumes at the same TR can be realized by increasing ES factor with increasing diffusion time. When TE, b-value and diffusion gradient length are also kept constant, this opens the possibility to explore the behavior of diffusion phenomena over different diffusion times. Figure 10 illustrates this with 2-shell diffusion data acquired at four diffusion times with otherwise matched parameters (i.e. TR, TE, δ and b-value are equal throughout, see Supplementary Table 3). Each 1.8 mm isotropic dataset had 24 directions at b = 1000s/mm^2, 48 directions at b = 2500s/mm^2 and 8 b_0's, for a total of 70 STE volumes (and 70 SE volumes, not shown). This is sufficient for whole-brain DTI analysis (on the b = 1000s/mm^2 shell, Figure 10B) and DKI analysis (on both shells) at each diffusion time (Figure 10C), and to assess how diffusion measures such as mean diffusivity (MD) and mean kurtosis (MK) change with diffusion time (Figure 10D).

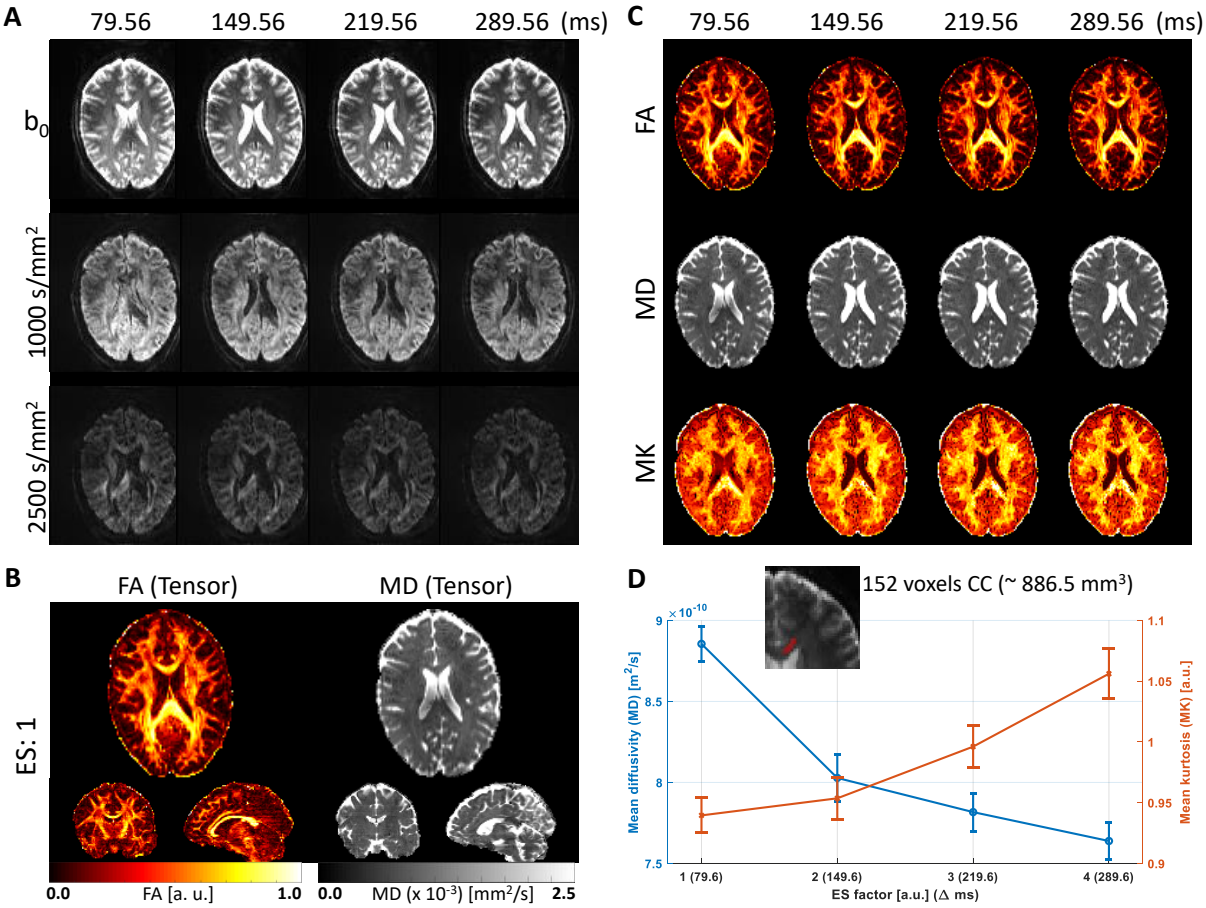

Figure 10: MESMERISED data and diffusion modeling results for STE volumes over several diffusion times at two b-values with matched TE and TR (TR = 3.50 s, TE = 45 ms) at 1.8 mm isotropic. (A) Example transverse slices through STE volumes at the two b-values and four diffusion times. (B) Whole-brain Tensor modeling resulting in FA and MD maps for the ES = 1 data (b = 1000 s/mm² shell only). (C) Tensor and Kurtosis modeling results (applied to suitable combinations of shells) for the different diffusion times. (D) Mean diffusivity (MD, blue) and Mean Kurtosis (MK, red) with their corresponding standard error plotted over ES factors/diffusion times for an ROI (red in the inset, with a total of 152 voxels along 10 slices) in the genu of the corpus callosum.

Discussion

MESMERISED achieves super-accelerated 7 T STEAM imaging by combining echo-shifting and multiband/simultaneous multi-slice acceleration, leading to very high multiplicative acceleration factors and time efficiency for qT_1 and diffusion imaging. Furthermore, qT_2 and B_1+ mapping can be performed with the same pulse sequence. MESMERISED inherits from STEAM the capacity to simultaneous generate both SE images and STE images and the possibility of performing qT_1, qT_2, B_1+ mapping as well as diffusion-weighted imaging. It also inherits the property of 50% lower SNR and 40% lower SAR compared to a similar spin-echo sequence, and 66% lower SAR compared to an inversion-prepared spin-echo sequence. In essence, MESMERISED capitalizes on the low SAR of the STEAM sequence to considerably increase its SNR per unit time through the multiplicative ESxMB acceleration. This enables fast multi-contrast mapping over the whole-brain, for instance at 1.8 mm isotropic, with qT_1 mapping (2:07), qT_2 mapping (1:48), B_1+ mapping (2:14) and 370 volume multi-shell diffusion (11:08), in a little over 17 minutes. Accepting a lower precision level in the quantitative maps (i.e. working with a single, rather than three repetitions), and 200 volumes in the diffusion dataset (cf. Supplementary Tables 1-3), would lower the total multi-contrast acquisition time to

under 10 minutes (i.e. qT_1 mapping in 1:18, qT_2 mapping 0:56, B_1+ mapping 1:05 and 200 volume multi-shell diffusion in 6:15).

qT_1 mapping

MESMERISED T_1 relaxometry can be performed at a low constant TR by increasing the ES factor proportionally to TM, which results in increasing total acceleration factors (e.g. from 3 to 36 in 1.8 mm data and from 3 to 54 in 1.25 mm data in Figure 4), highlighting the super-acceleration capability of MESMERISED for qT_1 imaging. Although the temporal speed-up of the multiplicative ESxMB acceleration is not linear with ES, the speed-up compared to multiband only accelerated STEAM can be very large (e.g. 6.02x faster than MB = 3 for 1.8 mm and 9.07x faster than MB = 3 for 1.25 mm). In addition, MESMERISED simultaneously provides spin-echo images in the same acquisition time, which can be used to either improve the precision of the qT_1 maps in the same acquisition time or achieve even shorter acquisition times for the same precision level. For instance, uncertainty in 1.25 mm isotropic qT_1 maps at a single repetition (acquisition time 1:40) with STE/SE ratio analysis are at similar levels as that of three repetitions (acquisition time 4:01) or even 5 repetitions (acquisition time 6:22) for STE-only analysis (Supplementary Figure 2, bottom row). Here it should be noted that these results are obtained at less than 100% duty cycle, with a doubling of the minimum achievable TR and TM (c.f. Supplementary Table 1, row 2 and 3), providing a better spacing and range of TM's for T_1 relaxometry. Potentially, in the future, this space can be used for simultaneous sampling of other contrasts, such as a multi-echo EPI readout (Poser and Norris, 2009) for qT_2/qT_2* mapping.

qT_2 and B_1+ mapping

Both qT_2 and B_1+ mapping can be performed over the whole-brain with MESMERISED (e.g. 1.8 mm isotropic qT_2 and B_1+ maps in roughly 2 minutes each; Figure 5B and 6C). Here we note that qT_2 and B_1+ mapping, per se, do not benefit from the accelerating echo-shifting capacity in MESMERISED. qT_2 and B_1+ mapping derive from basic properties of the STEAM sequence, i.e. relaxometry on SE or STE echo times and the α - $2\alpha - \alpha$ technique, respectively, which can be performed independently of any echo-shifting. However, the ability to perform qT_2 and B_1+ mapping with the same pulse sequence that provides highly accelerated qT_1 and diffusion imaging has considerable advantages for fast multi-contrast mapping. First, all quantitative contrasts are generated by the same sequence and readout train leading to similar image distortions which aid alignment of the different maps where needed. Second, for the same reason, the images from all contrasts share the same image noise distribution, which aids denoising with methods that take all images into account (Cordero-Grande et al., 2019; Veraart et al., 2016). Third, well-aligned B_1+ maps can help in correcting transmit field related biases in quantitative maps, for instance in qT_1 maps (Marques et al., 2010).

Diffusion MRI

For diffusion imaging MESMERISED inherits from STEAM the capacity to achieve long diffusion times and high b-values, as well as the possibility to simultaneously generate diffusion-weighted SE images and diffusion-weighted STE images. MESMERISED adds to this a very high data rate to explore a large range of b-values, diffusion directions, or diffusion times in a short time. For instance, 370 whole-brain diffusion volumes over 8 b-value shells up to b = 7000 s/mm^2 can be generated at 2 mm isotropic in 7 min and 47 s (ESxMB = 5x3), a data rate of almost a volume per second, or at 1.8 mm isotropic in 10 min and 53 s (ESxMB = 4x3; Figure 9A), a data rate of more than a volume per 2 seconds. In addition, this is achieved with a lower diffusion gradient duty cycle (as well as less gradient coil heating and accompanying cooling requirements) than PGSE, since the longer diffusion times in STEAM dictate shorter diffusion gradient durations for the same maximum b-value. The shells consist of one half SE volumes in low-b shells which can support analysis with Gaussian

diffusion models as in DTI, and one half STE volumes in the same number high-b shells which are suitable for non-Gaussian diffusion models, such as DKI, NODDI and CHARMED models. This provides a wealth of diffusion information from several different models in short acquisition time, which could be further extended in future work. For instance, instead of collecting a relatively large number of directions in 4 shells for each SE and STE, fewer (e.g. 6-12) directions could be acquired at each of many (e.g. 14-28) b-values. When carefully chosen, this would continue to support fitting of the aforementioned models on high-b STE volumes, while creating an opportunity to additionally fit the intra-voxel incoherent motion (IVIM) model (LeBihan, 1990) to the richly sampled low b-value domain in the SE volumes. Further tuning potential for the b-values of SE volumes (for a given STE max-b) lies in the choice of mixing time (and therefore diffusion time) of the STE volumes because, for the same TR and STE b-value, the SE b-value varies with different choices of TM and δ (see Supplementary Table 4).

The combination of high data rate and wide range of achievable diffusion times makes MESMERISED an excellent tool to investigate the behavior of diffusion phenomena at long and varying diffusion times. Several studies have shown that processes such as coarse-graining or exchange leave their mark in the change of diffusion MRI measures with increasing diffusion time (Burcaw et al., 2015; Nilsson et al., 2013; Novikov et al., 2014). Diffusion time-resolved dMRI can even be used to achieve some sensitivity to axonal diameter distributions (Alexander et al., 2010; Assaf et al., 2008; De Santis et al., 2016b). Most of these applications require quite extensive sampling of diffusion times, b-values and, sometimes, directions, often leading to long (e.g. 30 - 60 min) acquisitions with current techniques. MESMERISED can achieve time-efficient sampling of different diffusion times in the STE volumes at otherwise matched parameters by increasing ES factor with increasing diffusion time. We demonstrate this with 1.8 mm isotropic diffusion data acquired at four diffusion times from ~ 80 ms to ~ 290 ms, which supports both DTI and DKI at each diffusion time (Figure 10). The analysis of the resulting STE data with DTI and DKI captures a dependence of mean diffusivity and mean kurtosis with increasing diffusion time in white matter (Figure 10D), in agreement with earlier reports (Fieremans et al., 2016; Jespersen et al., 2018). In the future, MESMERISED could be a useful tool in further investigating such micro- and meso-structural phenomena. In principle, less than the number of directions acquired here per b-value (24 for b = 1000 s/mm^2, 48 for b = 2500 s/mm^2 at a total acquisition time of ~ 17 min for all diffusion times) might be sufficient for DKI and thus a shorter MESMERISED acquisition may be possible for this purpose. Furthermore, sampling higher diffusion times is a possibility, since correspondingly higher ES factors allow these to be acquired at the same TR (e.g. 430 ms at ES = 6 and 560 ms at ES = 8).

Outlook

As mentioned above, a useful extension will be a multi-echo EPI readout, which would enable further efficiency in mapping both qT_1 and qT_2/qT_2* since unused duty cycle in optimal-TM sampling for T_1 relaxometry can be used to sample multiple TE's per shot for T_2/T_2* relaxometry. This could potentially also make use of efficient sparse sampling trajectories of the temporal relaxation curve, such as in echo-planar time-resolved imaging (EPTI; Wang et al., 2019). A multi-echo readout would also enable further speed-up of mixed or dependent contrast sampling, such as mixed T_2/T_2* relaxometry and diffusion imaging (Tax, 2017; Veraart et al., 2018), and help characterise tissue compartments with separate relaxation constants and diffusion behavior (De Santis et al., 2016a; Hutter et al., 2018; Wu, 2017). Future combination with SAR efficient MB pulses, such as PINS (Norris et al., 2014; Norris et al., 2011), multi-PINS (Eichner et al., 2014) and pTx-MB (Poser et al., 2014; Wu et al., 2013) could allow high data quality at potentially even higher MB factors. For the fastest

acquisitions, acquisition of the reference data for GRAPPA and MB reconstruction takes a considerable proportion of the running time (about 30 s in the current implementation), which might be sped-up further with more efficient strategies. Additionally, a flexible table-based sequence looping implementation in which all parameters (TM, ES, TE, flip angles, diffusion direction and gradient amplitude) can be controlled independently, could allow running qT_1, qT_2, B_1+ and diffusion mapping in a single sequence run with a shared reference scan and reversed phase-encode direction scans, further decreasing the overhead time. Finally, the SAR efficiency of a STEAM-based sequence makes it very attractive for high duty cycle and multiband acceleration at 7 T, but many of the advantages could translate well to 3 T, particularly when MB factors are increased even further, as allowed by modern 32 to 64 channel head or head/neck RF-coils.

Conclusion

MESMERISED achieves super-accelerated 7 T STEAM imaging by combining echo-shifting and multiband/simultaneous multi-slice acceleration. This leads to very high multiplicative acceleration factors and time efficiency for qT_1 and diffusion imaging. MESMERISED can probe combined T_1, T_2 and diffusion contrast with high time efficiency for fast multi-contrast mapping and characterization of multi-component relaxometry, diffusion, and exchange.

Acknowledgements

AR and FJ were supported by an ERC Starting Grant (MULTICONNECT, #639938). AR was further supported by a Dutch science foundation (NWO) VIDI Grant (#14637). BP is partially funded by NWO VIDI Grant 016.Vidi.178.052. and NIH R01 MH111444/MH/NIMH.

Declaration of interest

AR, BP an FJ are co-inventors on a patent application related to the technique described in this manuscript.

References

Alexander, D.C., Hubbard, P.L., Hall, M.G., Moore, E.A., Ptito, M., Parker, G.J., Dyrby, T.B., 2010. Orientationally invariant indices of axon diameter and density from diffusion MRI. Neuroimage 52, 1374-1389.

Assaf, Y., Alexander, D.C., Jones, D.K., Bizzi, A., Behrens, T.E., Clark, C.A., Cohen, Y., Dyrby, T.B., Huppi, P.S., Knoesche, T.R., Lebihan, D., Parker, G.J., Poupon, C., consortium, C., Anaby, D., Anwander, A., Bar, L., Barazany, D., Blumenfeld-Katzir, T., De-Santis, S., Duclap, D., Figini, M., Fischi, E., Guevara, P., Hubbard, P., Hofstetter, S., Jbabdi, S., Kunz, N., Lazeyras, F., Lebois, A., Liptrot, M.G., Lundell, H., Mangin, J.F., Dominguez, D.M., Morozov, D., Schreiber, J., Seunarine, K., Nava, S., Poupon, C., Riffert, T., Sasson, E., Schmitt, B., Shemesh, N., Sotiropoulos, S.N., Tavor, I., Zhang, H.G., Zhou, F.L., 2013. The CONNECT project: Combining macro- and micro-structure. Neuroimage 80, 273-282.

Assaf, Y., Basser, P.J., 2005. Composite hindered and restricted model of diffusion (CHARMED) MR imaging of the human brain. Neuroimage 27, 48-58.

Assaf, Y., Blumenfeld-Katzir, T., Yovel, Y., Basser, P.J., 2008. AxCaliber: a method for measuring axon diameter distribution from diffusion MRI. Magn Reson Med 59, 1347-1354.

Assaf, Y., Freidlin, R.Z., Rohde, G.K., Basser, P.J., 2004. New modeling and experimental framework to characterize hindered and restricted water diffusion in brain white matter. Magn Reson Med 52, 965-978.

Assaf, Y., Pasternak, O., 2008. Diffusion tensor imaging (DTI)-based white matter mapping in brain research: a review. J Mol Neurosci 34, 51-61.

Basser, P.J., Mattiello, J., LeBihan, D., 1994. MR diffusion tensor spectroscopy and imaging. Biophys J 66, 259-267.

Beaulieu, C., 2002. The basis of anisotropic water diffusion in the nervous system - a technical review. NMR Biomed 15, 435-455.

Behrens, T.E., Berg, H.J., Jbabdi, S., Rushworth, M.F., Woolrich, M.W., 2007. Probabilistic diffusion tractography with multiple fibre orientations: What can we gain? Neuroimage 34, 144-155.

Behrens, T.E., Woolrich, M.W., Jenkinson, M., Johansen-Berg, H., Nunes, R.G., Clare, S., Matthews, P.M., Brady, J.M., Smith, S.M., 2003. Characterization and propagation of uncertainty in diffusion-weighted MR imaging. Magn Reson Med 50, 1077-1088.

Berman, S., Filo, S., Mezer, A.A., 2019. Modeling conduction delays in the corpus callosum using MRI-measured g-ratio. Neuroimage 195, 128-139.

Blazejewska, A.I., Bhat, H., Wald, L.L., Polimeni, J.R., 2017. Reduction of across-run variability of temporal SNR in accelerated EPI time-series data through FLEET-based robust autocalibration. Neuroimage 152, 348-359.

Breuer, F.A., Blaimer, M., Mueller, M.F., Seiberlich, N., Heidemann, R.M., Griswold, M.A., Jakob, P.M., 2006. Controlled aliasing in volumetric parallel imaging (2D CAIPIRINHA). Magn Reson Med 55, 549-556.

Burcaw, L.M., Fieremans, E., Novikov, D.S., 2015. Mesoscopic structure of neuronal tracts from time-dependent diffusion. Neuroimage 114, 18-37.

Callaghan, M.F., Helms, G., Lutti, A., Mohammadi, S., Weiskopf, N., 2015. A general linear relaxometry model of R1 using imaging data. Magn Reson Med 73, 1309-1314.

Campbell, J.S.W., Leppert, I.R., Narayanan, S., Boudreau, M., Duval, T., Cohen-Adad, J., Pike, G.B., Stikov, N., 2018. Promise and pitfalls of g-ratio estimation with MRI. Neuroimage 182, 80-96.

Cauley, S.F., Polimeni, J.R., Bhat, H., Wald, L.L., Setsompop, K., 2014. Interslice leakage artifact reduction technique for simultaneous multislice acquisitions. Magn Reson Med 72, 93-102.

Chung, S., Kim, D., Breton, E., Axel, L., 2010. Rapid B1+ mapping using a preconditioning RF pulse with TurboFLASH readout. Magn Reson Med 64, 439-446.

Cordero-Grande, L., Christiaens, D., Hutter, J., Price, A.N., Hajnal, J.V., 2019. Complex diffusion-weighted image estimation via matrix recovery under general noise models. Neuroimage 200, 391-404.

Cusack, R., Papadakis, N., 2002. New robust 3-D phase unwrapping algorithms: application to magnetic field mapping and undistorting echoplanar images. Neuroimage 16, 754-764.

De Santis, S., Assaf, Y., Jeurissen, B., Jones, D.K., Roebroeck, A., 2016a. T1 relaxometry of crossing fibres in the human brain. Neuroimage 141, 133-142.
De Santis, S., Drakesmith, M., Bells, S., Assaf, Y., Jones, D.K., 2014. Why diffusion tensor MRI does well only some of the time: variance and covariance of white matter tissue microstructure attributes in the living human brain. Neuroimage 89, 35-44.
De Santis, S., Jones, D.K., Roebroeck, A., 2016b. Including diffusion time dependence in the extra-axonal space improves in vivo estimates of axonal diameter and density in human white matter. Neuroimage 130, 91-103.
Ehses, P., Bause, J., Shajan, G., Scheffler, K., 2015. Efficient generation of T2*-weighted contrast by interslice echo-shifting for human functional and anatomical imaging at 9.4 Tesla. Magn Reson Med 74, 1698-1704.
Eichner, C., Wald, L.L., Setsompop, K., 2014. A low power radiofrequency pulse for simultaneous multislice excitation and refocusing. Magn Reson Med 72, 949-958.
Feinberg, D.A., Moeller, S., Smith, S.M., Auerbach, E., Ramanna, S., Gunther, M., Glasser, M.F., Miller, K.L., Ugurbil, K., Yacoub, E., 2010. Multiplexed echo planar imaging for sub-second whole brain FMRI and fast diffusion imaging. PLoS One 5, e15710.
Fieremans, E., Benitez, A., Jensen, J.H., Falangola, M.F., Tabesh, A., Deardorff, R.L., Spampinato, M.V., Babb, J.S., Novikov, D.S., Ferris, S.H., Helpern, J.A., 2013. Novel white matter tract integrity metrics sensitive to Alzheimer disease progression. AJNR Am J Neuroradiol 34, 2105-2112.
Fieremans, E., Burcaw, L.M., Lee, H.H., Lemberskiy, G., Veraart, J., Novikov, D.S., 2016. In vivo observation and biophysical interpretation of time-dependent diffusion in human white matter. Neuroimage 129, 414-427.
Frahm, J., Merboldt, K.D., Hänicke, W., Haase, A., 1985. Stimulated echo imaging. Journal of Magnetic Resonance (1969) 64, 81-93.
Fukunaga, M., Li, T.Q., van Gelderen, P., de Zwart, J.A., Shmueli, K., Yao, B., Lee, J., Maric, D., Aronova, M.A., Zhang, G., Leapman, R.D., Schenck, J.F., Merkle, H., Duyn, J.H., 2010. Layer-specific variation of iron content in cerebral cortex as a source of MRI contrast. Proc Natl Acad Sci U S A 107, 3834-3839.
Gibson, A., Peters, A.M., Bowtell, R., 2006. Echo-shifted multislice EPI for high-speed fMRI. Magn Reson Imaging 24, 433-442.
Griswold, M.A., Jakob, P.M., Heidemann, R.M., Nittka, M., Jellus, V., Wang, J., Kiefer, B., Haase, A., 2002. Generalized autocalibrating partially parallel acquisitions (GRAPPA). Magn Reson Med 47, 1202-1210.
Harms, R.L., Fritz, F.J., Schoenmakers, S., Roebroeck, A., 2019. Fast quantification of uncertainty in non-linear diffusion MRI models for artifact detection and more power in group studies. bioRxiv, 651547.
Harms, R.L., Fritz, F.J., Tobisch, A., Goebel, R., Roebroeck, A., 2017. Robust and fast nonlinear optimization of diffusion MRI microstructure models. Neuroimage 155, 82-96.
Hutter, J., Slator, P.J., Christiaens, D., Teixeira, R., Roberts, T., Jackson, L., Price, A.N., Malik, S., Hajnal, J.V., 2018. Integrated and efficient diffusion-relaxometry using ZEBRA. Sci Rep 8, 15138.
Ivanov, D., Schafer, A., Streicher, M.N., Heidemann, R.M., Trampel, R., Turner, R., 2010. A simple low-SAR technique for chemical-shift selection with high-field spin-echo imaging. Magn Reson Med 64, 319-326.
Jelescu, I.O., Veraart, J., Adisetiyo, V., Milla, S.S., Novikov, D.S., Fieremans, E., 2015. One diffusion acquisition and different white matter models: how does microstructure change in human early development based on WMTI and NODDI? Neuroimage 107, 242-256.
Jenkinson, M., Beckmann, C.F., Behrens, T.E., Woolrich, M.W., Smith, S.M., 2012. Fsl. Neuroimage 62, 782-790.
Jensen, J.H., Helpern, J.A., Ramani, A., Lu, H., Kaczynski, K., 2005. Diffusional kurtosis imaging: the quantification of non-gaussian water diffusion by means of magnetic resonance imaging. Magn Reson Med 53, 1432-1440.
Jespersen, S.N., Olesen, J.L., Hansen, B., Shemesh, N., 2018. Diffusion time dependence of microstructural parameters in fixed spinal cord. Neuroimage 182, 329-342.

Jones, D.K., 2004. The effect of gradient sampling schemes on measures derived from diffusion tensor MRI: a Monte Carlo study. Magn Reson Med 51, 807-815.
Jones, D.K., Knosche, T.R., Turner, R., 2013. White matter integrity, fiber count, and other fallacies: the do's and don'ts of diffusion MRI. Neuroimage 73, 239-254.
LeBihan, D., 1990. IVIM method measures diffusion and perfusion. Diagn Imaging (San Franc) 12, 133, 136.
Li, K., Li, H., Zhang, X.Y., Stokes, A.M., Jiang, X., Kang, H., Quarles, C.C., Zu, Z., Gochberg, D.F., Gore, J.C., Xu, J., 2016. Influence of water compartmentation and heterogeneous relaxation on quantitative magnetization transfer imaging in rodent brain tumors. Magn Reson Med 76, 635-644.
Lu, L., Erokwu, B., Lee, G., Gulani, V., Griswold, M.A., Dell, K.M., Flask, C.A., 2012. Diffusion-prepared fast imaging with steady-state free precession (DP-FISP): a rapid diffusion MRI technique at 7 T. Magn Reson Med 68, 868-873.
Lutti, A., Dick, F., Sereno, M.I., Weiskopf, N., 2014. Using high-resolution quantitative mapping of R1 as an index of cortical myelination. Neuroimage 93 Pt 2, 176-188.
Lutti, A., Stadler, J., Josephs, O., Windischberger, C., Speck, O., Bernarding, J., Hutton, C., Weiskopf, N., 2012. Robust and fast whole brain mapping of the RF transmit field B1 at 7T. PLoS One 7, e32379.
Marques, J.P., Kober, T., Krueger, G., van der Zwaag, W., Van de Moortele, P.F., Gruetter, R., 2010. MP2RAGE, a self bias-field corrected sequence for improved segmentation and T1-mapping at high field. Neuroimage 49, 1271-1281.
Moeller, S., Yacoub, E., Olman, C.A., Auerbach, E., Strupp, J., Harel, N., Ugurbil, K., 2010. Multiband multislice GE-EPI at 7 tesla, with 16-fold acceleration using partial parallel imaging with application to high spatial and temporal whole-brain fMRI. Magn Reson Med 63, 1144-1153.
Nilsson, M., van Westen, D., Stahlberg, F., Sundgren, P.C., Latt, J., 2013. The role of tissue microstructure and water exchange in biophysical modelling of diffusion in white matter. MAGMA 26, 345-370.
Norris, D.G., Boyacioglu, R., Schulz, J., Barth, M., Koopmans, P.J., 2014. Application of PINS radiofrequency pulses to reduce power deposition in RARE/turbo spin echo imaging of the human head. Magn Reson Med 71, 44-49.
Norris, D.G., Koopmans, P.J., Boyacioglu, R., Barth, M., 2011. Power Independent of Number of Slices (PINS) radiofrequency pulses for low-power simultaneous multislice excitation. Magn Reson Med 66, 1234-1240.
Novikov, D.S., Jensen, J.H., Helpern, J.A., Fieremans, E., 2014. Revealing mesoscopic structural universality with diffusion. Proc Natl Acad Sci U S A 111, 5088-5093.
O'Brien, K.R., Kober, T., Hagmann, P., Maeder, P., Marques, J., Lazeyras, F., Krueger, G., Roche, A., 2014. Robust T1-weighted structural brain imaging and morphometry at 7T using MP2RAGE. PLoS One 9, e99676.
Panagiotaki, E., Schneider, T., Siow, B., Hall, M.G., Lythgoe, M.F., Alexander, D.C., 2012. Compartment models of the diffusion MR signal in brain white matter: a taxonomy and comparison. Neuroimage 59, 2241-2254.
Pierpaoli, C., Jezzard, P., Basser, P.J., Barnett, A., Di Chiro, G., 1996. Diffusion tensor MR imaging of the human brain. Radiology 201, 637-648.
Poser, B.A., Anderson, R.J., Guerin, B., Setsompop, K., Deng, W., Mareyam, A., Serano, P., Wald, L.L., Stenger, V.A., 2014. Simultaneous multislice excitation by parallel transmission. Magn Reson Med 71, 1416-1427.
Poser, B.A., Norris, D.G., 2009. Investigating the benefits of multi-echo EPI for fMRI at 7 T. Neuroimage 45, 1162-1172.
Santis, S., Assaf, Y., Evans, C.J., Jones, D.K., 2014. Improved precision in CHARMED assessment of white matter through sampling scheme optimization and model parsimony testing. Magn Reson Med 71, 661-671.

Setsompop, K., Gagoski, B.A., Polimeni, J.R., Witzel, T., Wedeen, V.J., Wald, L.L., 2012. Blipped-controlled aliasing in parallel imaging for simultaneous multislice echo planar imaging with reduced g-factor penalty. Magn Reson Med 67, 1210-1224.

Stuber, C., Morawski, M., Schafer, A., Labadie, C., Wahnert, M., Leuze, C., Streicher, M., Barapatre, N., Reimann, K., Geyer, S., Spemann, D., Turner, R., 2014. Myelin and iron concentration in the human brain: a quantitative study of MRI contrast. Neuroimage 93 Pt 1, 95-106.

Tax, C.M.W.R., U.S.; Witzel, T.; Jones, D.K., 2017. Disentangling in two dimensions in the living human brain: Feasbilty of relaxometry-diffusometry using ultra-strong gradients. ISMRM 25th Annual Meeting & Exhibition, Honolulu, HI, USA.

Teeuwisse, W.M., Brink, W.M., Webb, A.G., 2012. Quantitative assessment of the effects of high-permittivity pads in 7 Tesla MRI of the brain. Magn Reson Med 67, 1285-1293.

Tournier, J.D., Smith, R., Raffelt, D., Tabbara, R., Dhollander, T., Pietsch, M., Christiaens, D., Jeurissen, B., Yeh, C.H., Connelly, A., 2019. MRtrix3: A fast, flexible and open software framework for medical image processing and visualisation. Neuroimage 202, 116137.

Veraart, J., Novikov, D.S., Christiaens, D., Ades-Aron, B., Sijbers, J., Fieremans, E., 2016. Denoising of diffusion MRI using random matrix theory. Neuroimage 142, 394-406.

Veraart, J., Novikov, D.S., Fieremans, E., 2018. TE dependent Diffusion Imaging (TEdDI) distinguishes between compartmental T2 relaxation times. Neuroimage 182, 360-369.

Vu, A.T., Auerbach, E., Lenglet, C., Moeller, S., Sotiropoulos, S.N., Jbabdi, S., Andersson, J., Yacoub, E., Ugurbil, K., 2015. High resolution whole brain diffusion imaging at 7T for the Human Connectome Project. Neuroimage 122, 318-331.

Wang, F., Dong, Z., Reese, T.G., Bilgic, B., Katherine Manhard, M., Chen, J., Polimeni, J.R., Wald, L.L., Setsompop, K., 2019. Echo planar time-resolved imaging (EPTI). Magn Reson Med 81, 3599-3615.

Weiskopf, N., Suckling, J., Williams, G., Correia, M.M., Inkster, B., Tait, R., Ooi, C., Bullmore, E.T., Lutti, A., 2013. Quantitative multi-parameter mapping of R1, PD(*), MT, and R2(*) at 3T: a multi-center validation. Frontiers in neuroscience 7, 95.

Wu, H.T., Q.; Poetter, C.; Zhu, K.; Middione, M.; Kerr, A.B.; McNab, J.A.; Dougherty, R., 2017. Whole Brain Inversion Recovery Diffusion Weighted Imaging Using Slice-Shuffled Acquisition. ISMRM 25th Annual Meeting & Exhibition, Honolulu, HI, USA.

Wu, X., Schmitter, S., Auerbach, E.J., Moeller, S., Ugurbil, K., Van de Moortele, P.F., 2013. Simultaneous multislice multiband parallel radiofrequency excitation with independent slice-specific transmit B1 homogenization. Magn Reson Med 70, 630-638.

Zhang, H., Hubbard, P.L., Parker, G.J., Alexander, D.C., 2011. Axon diameter mapping in the presence of orientation dispersion with diffusion MRI. Neuroimage 56, 1301-1315.

Zhang, H., Schneider, T., Wheeler-Kingshott, C.A., Alexander, D.C., 2012. NODDI: practical in vivo neurite orientation dispersion and density imaging of the human brain. Neuroimage 61, 1000-1016.